https://doi.org/10.5194/egusphere-2025-5371
Preprint. Discussion started: 7 November 2025

Observed multiscale dynamical processes responsible for an extreme wind gust event in Beijing

Xiaoran Guo[a,b], Jianping Guo[a*], Ning Li[a], Zhen Zhang[a,c], Tianmeng Chen[a], Yu Shi[d], Pengzhan Yao[a,c], Shuairu Jiang[a], Lei Zhao[b], Fei Hu[d]

[a]State Key Laboratory of Severe Weather Meteorological Science and Technology & Specialized Meteorological Support Technology Research Center, Chinese Academy of Meteorological Sciences, Beijing 100081, China

[b] Key Laboratory of South China Sea Meteorological Disaster Prevention and Mitigation of Hainan Province, Haikou 570203, China

[c] Department of Atmospheric and Oceanic Sciences and Institute of Atmospheric Sciences, Fudan University, Shanghai 200438, China

[d] State Key Laboratory of Atmospheric Environment and Extreme Meteorology, Institute of Atmospheric Physics, Chinese Academy of Sciences, Beijing 100029, China

*Correspondence to:

Dr./Prof. Jianping Guo (Email: jpguocams@gmail.com)

https://doi.org/10.5194/egusphere-2025-5371
Preprint. Discussion started: 7 November 2025

Abstract

Extreme wind gusts pose substantial threats to human safety and infrastructure, yet pre-onset observational constraints remain inadequate, leading to large uncertainties and inaccuracies in nowcasting and prediction. To address this gap, we conduct an in-depth investigation of a record-breaking surface gust event (wind speed >35 m s^{-1}) that occurred in Beijing during the early afternoon of 30 May 2024. We explore the dynamical characteristics of this event utilizing a high-resolution meteorological mesonet, which includes seven radar wind profilers, a meteorological tower, automated weather stations, radar and satellite data. Multi-source observational analyses show the development of multicellular storm ahead of the convergence line as the northeasterly cold outflows met environmental southerly winds during its downhill propagation. Evaporative cooling contributed to the generation of the extreme winds through the downward momentum transport and pressure gradient forcing. After reaching the plain, two convective segments subsequently merged into a well-organized squall system embedded with a midlevel mesovortex with intense rear-inflow jet. The emergence of low-level frontogenesis and shearing deformation provided favorable conditions for sustaining mesoscale convection. This mesoscale convection then fueled small-scale turbulent energy processes. The inverse energy cascades of turbulence — a process involving energy transfer from small to large eddies — significantly intensified as wind speeds increased markedly. This study offers valuable insights into the multiscale dynamical processes governing extreme gust wind events. Moreover, these findings underscore the value of RWP mesonet observations for enhancing our understanding of extreme wind events and in improving the nowcasting and prediction efforts in the future.

Key words: Extreme winds, Radar wind profilers, Quasi-linear convective systems, Turbulence

https://doi.org/10.5194/egusphere-2025-5371
Preprint. Discussion started: 7 November 2025

1. Introduction

Extreme intense winds rank among the most destructive meteorological hazards globally, causing cascading disasters such as infrastructure collapse, wildfire escalation, and aviation accidents (Goyette, 2003; Peterson et al., 2014; Pryor and Barthelmie, 2010; 2011). However, large uncertainties in the wind speed estimations still exist in weather forecast models and reanalysis products (Azorin-Molina et al., 2016; Hirt & Craig, 2021; Kahl, 2020; Pryor and Barthelmie, 2021; Torralba et al., 2017; Wu et al., 2024), especially for those associated with convection-induced extreme wind gusts, due partly to limitations in spatial resolution and parameterization schemes (Adams-Selin et al., 2013; Burghardt et al., 2014; Fiori et al., 2011; Fovell, 2002).

Wind gusts—short-lived extreme events—arise when air with high momentum is transported to the surface (Harris & Kahl, 2017). They occur alongside both convective and nonconvective processes and are affected by a range of physical factors, including wind speed, turbulence in the planetary boundary layer (PBL), topographic flows and surface roughness (Letson et al., 2018). Regarding the convection-induced wind gust the role of a complex interplay of factors has been well recognized, such as mesoscale dynamics and thermodynamics interaction (Abulikemu et al., 2019; Johns & Hirt 1987; Taszarek et al., 2019; Vose et al., 2014), turbulence-convection interaction (Shao et al., 2023a; 2023b; Tang et al., 2015; Tucker et al., 2009), and microphysics processes and dynamics interactions (Adams-Selin et al. 2013; Mahoney and Lackmann 2011; Zhou et al. 2020).

Among others, quasi-linear convective systems (QLCSs) such as squall lines can produce a straight-line swath of extreme winds (Coniglio et al., 2011; Fujita 1978; Johns & Hirt 1987; Meng et al. 2012; Xu et al., 2024). Given their damaging potential, many efforts have been made in the past few decades to explore the mechanisms of extreme wind gusts generated by QLCSs in observational and numerical studies (e.g., Atkins et al., 2005; Bentley & Mote, 1998; Meng et al. 2012; Lafore and Moncrieff 1989). It was consistently found that the intensity of cold outflows is one of the main

https://doi.org/10.5194/egusphere-2025-5371
Preprint. Discussion started: 7 November 2025

contributors of extreme wind gusts (Chen et al., 2024; Haerter et al., 2019; Houze, 2014). The formation of mesoscale vortices (Atkins & Laurent, 2009; Evans et al., 2014; Wheatley & Trapp 2008; Xu et al., 2015b; Zhang et al., 2021) and the merger of convective cells (French and Parker; 2012; 2014; Liu et al., 2023) have a close connection with the evolution of QLCSs and the initiation of extreme wind gusts. The midlevel rear-inflow jet (RIJ) in the stratiform region of QLCSs plays an important role in strengthening the extreme winds at the surface via the downward transport of momentum (Grim et al., 2009; Weisman, 1992; Xu et al., 2015a; Zhang & Gao 1989).

Although the above-mentioned studies have made some progress in quantifying the characteristics of QLCSs, reliable QLCS-induced gust forecasting remains challenging to achieve. This is mainly because the energy-carrying turbulent eddies that harbor gusts are typically far too small to be resolved by observational networks and mesoscale numerical models (Fovell and Cao, 2014). To the best of our knowledge, most previous studies, nevertheless, relied on a model simulation or reanalyses. This leads to large knowledge gaps in the vertical structure of the lower troposphere and its evolution in the presence of QLCS, especially for highly localized and transient storms (Luchetti et al., 2020; Romanic et al., 2020). As such, more studies are urgently needed to elucidate the multiple scales of interaction for an in-depth understanding of the formation mechanisms that create extreme wind gust events. In this regard, detailed vertical observations are essential for capturing the dynamic structure and evolving convective morphology leading to damaging winds (Bélair et al., 2025). High-density continuous vertical measurements of wind profiles provided by ground-based mesonet observations, including radar wind profiler (RWP) and meteorological towers, afford us a valuable perspective to shed light on these complex phenomena.

Here we examine an extreme wind gust event associated with a QLCS that occurred in Beijing on 30 May 2024. The instantaneous surface wind speeds at 250 sites in this event exceeded 17.2 m s^{-1} with the maximum wind speed reaching 37.2 m s^{-1}. This high-wind-producing convective system caused widespread fallen trees and

https://doi.org/10.5194/egusphere-2025-5371
Preprint. Discussion started: 7 November 2025

power lines, damaging many vehicles and buildings. Here, this intense wind gust event is comprehensively analyzed by using a high-resolution meteorological mesonet consisting of seven RWPs and one meteorological tower in an attempt to gain insight into the vertical structural evolution within the PBL and elucidate the complex multi-scale dynamical processes during the event. The next section describes the data and methodology used in this work. Section 3 presents an overview of the QLCS and associated extreme wind gust event. In Section 4, the utility of the RWPs and meteorological tower mesonet in capturing the evolving vertical structure of the high-wind event is examined. Key findings are concluded in the final section.

2. Data and Methodology

2.1 Vertical profile measurements

Figure 1a presents the spatial distribution of RWP mesonet deployed in Beijing, which is composed of the following six stations: Haidian (HD; 39.98°N, 116.28°E), Huairou (HR; 40.36°N, 116.63°E), Yanqing (YQ; 40.45°N, 115.97°E), Shangdianzi (SDZ; 40.66°N, 117.11°E), Pinggu (PG; 40.17°N, 117.12°E), Xiayunling (XYL; 39.73° N, 115.74°E), and the Beijing Weather Observatory (BWO; 39.79°N, 116.47°E). These RWPs are Ce Feng Leida-6 (CFL-6) Tropospheric Wind Profilers, which are produced by the 23rd Institute of China Aerospace Science and Industry Corporation (Liu et al., 2020).

They provide measurements of horizontal and vertical winds, and refractive index structure parameter at 6-min intervals. The vertical resolution is 120 m from 0.15 to 4.11 km above the ground level (AGL) in low-operating mode, and 240 m from 4.11 to 10.11 km AGL in high-operating mode. After testing the data quality of the RWPs in our previous study (Guo et al., 2023), horizontal wind speed, direction and vertical velocity derived from RWPs in the heights of 0.51–4.95 km AGL were found to be

https://doi.org/10.5194/egusphere-2025-5371
Preprint. Discussion started: 7 November 2025

reliable. Linear interpolation in time is adopted to fill missing values for the continuity of data.

Upper-air sounding balloons launched at the Zhangjiakou (ZJK; 40.77°N, 114.92° E) and Beijing Weather Observatory (BWO) sites at 0800 and 2000 local standard time (LST) on 30 May 2024 are used to provide the vertical profiles of thermodynamic features, including temperature, pressure, relative humidity, and horizontal winds with a vertical resolution of 5–8 m (Guo et al., 2021).

The 325-meter-high meteorological tower is located at 39.97°N, 116.37°E, at an elevation of 49 m above mean sea level (AMSL). Seven sets of three-dimensional ultrasonic anemometers are installed at seven different heights of the tower: 8, 15, 47, 80, 140, 200 and 280 m, which are used to measure horizontal wind speed, direction, and vertical velocity with a sampling frequency of 10 Hz. These measurements have undergone strict data quality checks; refer to Shi and Hu (2020) and Shi et al. (2020) for more details.

2.2 Radar reflectivity and surface meteorological observations

Identifying and tracking of the mesoscale convective system (MCS) is conducted using a composite radar reflectivity with a resolution of approximately 0.01° in both latitude and longitude derived from the China Meteorological Administration (CMA) Doppler radar network. It integrates the maximum reflectivity measurements from the Doppler weather radars at each pixel across different levels. To better characterize the propagation of a gust front, the Doppler radar radial velocity from the S-band Doppler radar at BWO is also used.

Ground-based meteorological variables are also used in the analysis over the study area, including 2 m air temperature (T_{2m}), relative humidity, and pressure measured at 5 min intervals, as well as instantaneous 10 m wind speed (WS_{10m}), wind direction, and precipitation measured at 1 min intervals from automated weather stations (AWSs).

https://doi.org/10.5194/egusphere-2025-5371
Preprint. Discussion started: 7 November 2025

2.3 Reanalysis and satellite datasets

ERA5 is the fifth-generation atmospheric reanalysis of ECMWF (European Centre for Medium-Range Weather Forecasts), which benefits from advancements in data assimilation, model physics and dynamics (Hersbach et al., 2023). The ERA5 dataset can provide meteorological parameters on 37 pressure levels with a spatial resolution of 0.25°×0.25° at hourly intervals. The geopotential height, temperature, relative humidity, and horizontal wind fields at 500 hPa and 850 hPa are used to analyze the large-scale conditions prior to the severe wind gust event in Beijing.

Himawari-8/9 is one of the next-generation geostationary satellites operated by the Japan Meteorological Agency, which was launched on 7 October 2014 and located at 140.7°E, 0°N (Da, 2015). It has provided real-time observations to the public since 7 July 2015 (ftp://ftp.ptree.jaxa.jp/jma) with diverse central wavelengths (from 0.47 to 13.3 μm). In this study, we use brightness temperature from the 10.8 μm-channel high-resolution geostationary satellite Himawari-8/9 (L1 gridded data) to identify and track MCSs at 10-minute intervals. The data have a spatial resolution of 0.25° × 0.25° (Bessho et al., 2016; Chen et al., 2019).

2.4 Calculation of divergence, vorticity, stretching and shearing deformation

Divergence, vorticity, stretching and shearing are four fundamental air motion diagnostics (Yanai and Nitta, 1967; Brandes and Ziegler, 1993, Shapiro et al., 2009). The horizontal divergence D and vertical vorticity ζ respectively reflect the area change and rotation of the air parcel (Bony & Stevens, 2019; Lenschow et al., 2007). Stretching and shearing deformations, denoted S_1 and S_2 here, result in elongation parallel to the axis of dilatation and contraction orthogonal to it. Stretching deformation can flatten and lengthen the air parcel, while shearing deformation can twist the air parcel in two perpendicular directions.

Generally, these four different motions above can be represented by pairs of partial derivatives of velocity $\frac{\partial u}{\partial x}+\frac{\partial v}{\partial y}$, $\frac{\partial v}{\partial x}-\frac{\partial u}{\partial y}$, $\frac{\partial u}{\partial x}-\frac{\partial v}{\partial y}$ and $\frac{\partial v}{\partial x}+\frac{\partial u}{\partial y}$. The triangle method, as proposed by Bellamy (1949), computes the divergence based on the rate of change

https://doi.org/10.5194/egusphere-2025-5371
Preprint. Discussion started: 7 November 2025

in a fluid triangle initially coincident with the network composed by any three points *A, B,* and *C*. The triangle-area averaged horizontal divergence *D* and vertical vorticity ζ can be computed by the triangle method as follows

$$D=\frac{(u_B-u_A)(y_C-y_A)-(u_c-u_A)(y_B-y_A)+(x_B-x_A)(v_C-v_A)-(x_c-x_A)(v_B-v_A)}{(x_B-x_A)(y_C-y_A)-(x_c-x_A)(y_B-y_A)}, \quad (1)$$

$$\zeta=\frac{(v_B-v_A)(y_C-y_A)-(v_c-v_A)(y_B-y_A)-(x_B-x_A)(u_C-u_A)+(x_c-x_A)(u_B-u_A)}{(x_B-x_A)(y_C-y_A)-(x_c-x_A)(y_B-y_A)}, \quad (2)$$

Here, $(x_i,y_i)(i=A,B,C)$ are the location of three vortex points, $\vec{V_i}=(u_i,v_i)$ are the zonal and meridional component of horizontal wind, respectively.

Analogously, the stretching and shearing deformation can be derived using the following equations:

$$S_1=\frac{(u_B-u_A)(y_C-y_A)-(u_c-u_A)(y_B-y_A)-(x_B-x_A)(v_C-v_A)+(x_c-x_A)(v_B-v_A)}{(x_B-x_A)(y_C-y_A)-(x_c-x_A)(y_B-y_A)}, \quad (3)$$

$$S_2=\frac{(v_B-v_A)(y_C-y_A)-(v_c-v_A)(y_B-y_A)+(x_B-x_A)(u_C-u_A)-(x_c-x_A)(u_B-u_A)}{(x_B-x_A)(y_C-y_A)-(x_c-x_A)(y_B-y_A)}, \quad (4)$$

To meet the consistency in shape and area, four triangles from west to east are constructed based on the positions of six RWPs deployed at YQ, XYL, HR, BWO, PG and SDZ. Considering the six RWPs located at different terrain elevations, the horizontal and vertical velocities measured by each RWP are interpolated to the same altitude that starts upwards from 0.51 km to 4.95 km above mean sea level (AMSL) with a vertical resolution of 120 m.

2.5 Calculation of frontogenesis function

As mentioned above, four air motion types may cause some parts of the air parcel to move away from each other and some parts of the air parcel to move towards each other, resulting in frontolysis and frontogenesis respectively (Miller, 1948). Previous studies have used the frontogenesis function *F* to infer the evolution of horizontal temperature gradient (Bluestein, 1986), which contains the following four terms:

$$F=\frac{d}{dt}\left|\nabla_h\theta_e\right|=F_1+F_2+F_3+F_4, \quad (5)$$

https://doi.org/10.5194/egusphere-2025-5371
Preprint. Discussion started: 7 November 2025

$$F_1 = -\frac{1}{2} D\left|\nabla_h \theta_e\right|, \tag{6}$$

$$F_2 = -\frac{1}{2}\left[S_1\left(\frac{\partial \theta_e}{\partial x}\right)^2 + 2S_2\left(\frac{\partial \theta_e}{\partial x}\right)\left(\frac{\partial \theta_e}{\partial y}\right) - S_1\left(\frac{\partial \theta_e}{\partial y}\right)^2\right] / \left|\nabla_h \theta_e\right|, \tag{7}$$

$$F_3 = \left(\frac{\partial \theta_e}{\partial x}\frac{\partial Q}{\partial x} + \frac{\partial \theta_e}{\partial y}\frac{\partial Q}{\partial y}\right) / \left|\nabla_h \theta_e\right|, \tag{8}$$

$$F_4 = -\left(\frac{\partial \theta_e}{\partial x}\frac{\partial w}{\partial x} + \frac{\partial \theta_e}{\partial y}\frac{\partial w}{\partial y}\right)\frac{\partial \theta_e}{\partial z} / \left|\nabla_h \theta_e\right|, \tag{9}$$

where ∇_h is the horizontal Hamilton operator, θ_e is equivalent potential temperature, Q is diabatic heating, w is vertical velocity. The four terms characterize the effects of horizontal divergence, horizontal deformation, diabatic heating and vertical motion on frontogenesis. Frontogenesis occurs if F is larger than zero. Since the variability of vertical velocity along the horizontal direction is quite small, F_4 is not included in the calculation (Han et al., 2021). D, S_1 and S_2 in the preceding subsection from the RWP mesonet are then applied to these equations in order to calculate the vertical profile of F. Limited by the lack of vertical profiles of thermal parameters in real-time, the gradients of θ_e are obtained from surface observations from AWSs in Beijing.

2.6 Identification of inverse energy cascade

The direction of the turbulent energy cascade is determined by the sign of the energy flux ε, which is calculated based on the third moment of the velocity difference (Shao et al., 2022):

$$\varepsilon = -\frac{2}{3}\frac{\left\langle\left[u_r(x+r) - u_r(x)\right]^3\right\rangle}{r}, \tag{10}$$

where r is the distance along any direction, u_r is the velocity parallel to r, and the angular bracket denotes the ensemble mean. When applying Eq. (10) in the vertical direction, it can be rewritten as:

$$\varepsilon = -\frac{2}{3}\frac{\left\langle\left[w(z+\Delta z) - w(z)\right]^3\right\rangle}{\Delta z}, \tag{11}$$

https://doi.org/10.5194/egusphere-2025-5371
Preprint. Discussion started: 7 November 2025

where w is the vertical velocity derived from the three-dimensional ultrasonic anemometer at one height z, Δz denotes the height difference between the upper height and z. Positive and negative ε indicate direct and inverse energy cascade (IEC), respectively. IEC is generally identified when $\varepsilon < -0.002\ m^2 \cdot s^{-3}$ to minimize the impact of observational errors on the results (Zhou et al., 2025).

3. Case overview

In the afternoon of 30 May 2024, an extreme wind event occurred as a downhill thunderstorm propagated eastward and entered the plain. During the evolution of the MCS, a number of high winds (instantaneous 10 m wind speed $\geqslant$ 17.2 m s^{-1}) were observed by automatic weather stations in Beijing after 1330 LST (Fig. 2a). High winds mainly occurred in the western mountainous areas of Beijing from 1400 to 1429 LST during the downhill progress of the developing MCS (Fig. 2b), with the maximum instantaneous 10 m wind speed of 37.2 m s^{-1} detected at the Qianling Mountain site (39.87°N, 116.07°E). After 1430 LST, both rainfall and the number of stations recording high winds increased remarkably (Fig. 2c) associated with the merger of two convective segments and formation of the squall line. At the mature stage of squall line (Fig. 2d), the wind gust coincided with the intensification of deep convection with the maximum rainfall exceeding 9 mm during 1500-1529 LST along the leading line, after which the squall line moved eastward away from the major urban area of Beijing.

3.1 Synoptic background

Figure 3a-b shows the large-scale conditions at 1300 BJT prior to the extreme wind gust event. Significant cold advection with the northwesterly jet exceeding 20 m s^{-1} was found over Beijing that was associated with a deep northeast cold vortex at 500 hPa. Meanwhile, Beijing was situated in the warm sector with temperature exceeding 15°C at 850 hPa (Fig. 3b). The steep midlevel lapse rate of temperature provides a favorable environment for deepening organization of convection and releasing unstable energy. A short-wave trough with horizontal wind shear appeared to the west of Beijing at 850

https://doi.org/10.5194/egusphere-2025-5371
Preprint. Discussion started: 7 November 2025

hPa (Fig. 3b), indicating the important dynamic contribution to the subsequent deepening organization of convection.

Unfortunately, no sounding was available to elucidate the temporal evolution of thermal stratification during the gusty wind event. We can only indicate the pre-storm environment by the soundings at 0800 LST from the radiosonde at the ZJK and BWO sites, respectively (see Fig. 3c, d). Consistent with the ERA5 reanalysis data, the sounding at the ZJK revealed upstream conditions in which thunderstorms were likely to develop (Fig. 3c). These conditions consist of a strong northwesterly wind at mountaintop level, increasing with height and oriented perpendicular to the Mt. Taihang range throughout a deep layer (Chen et al., 2012; 2014; Guo et al., 2024; Xiao et al., 2017; 2019; Li et al., 2017; Wilson et al., 2010).

The veering of the northerly wind to a westerly wind from 850 hPa to above 400 hPa also indicated the presence of cold advection at the BWO. The Skew T-logP diagram at the BWO shows moderate convective available potential energy (CAPE) of 460.5 J kg^{-1} and convective inhibition (CIN) of 114.4 kg^{-1}. A deep dry layer was seen from the surface to about 350 hPa with low-level humidity less than 60%. This dry column provided a favorable environment for the evaporation of precipitation particles from the moving storm. This intense evaporative cooling might have enhanced cold downdraft air, thus leading to the generation of the wind gust event. After the passage of the MCS, a surface-based temperature inversion layer below 880 hPa with larger CIN was captured by the sounding at 2000 LST due to the heat release (not shown). Westerly winds controlled the near-surface layer and gradually changed upward to northwesterly at 700 hPa, implying some warm advection in some degrees.

3.2 Evolution of the QLCS

Figure 4 shows the Hiamwari-8 10.8 μm brightness temperature, superimposed with mosaic composite radar reflectivity during the different stage of the QLCS. At the same time, the evolution of 30-minute perturbations of T_{2m} (ΔT_{2m}), superimposed with 30-minute perturbations of pressure (ΔP), is displayed in Fig. 5. It is evident from Fig. 4a that relatively dry conditions and few clouds covered much of the plain in the early

https://doi.org/10.5194/egusphere-2025-5371
Preprint. Discussion started: 7 November 2025

afternoon of 30 May. Furthermore, the plain was dominated by a surface south-to-southwesterly flow (Fig. 5a). A circular-shaped cloud cluster with more intense convective activity, denoted as C1, propagated eastward and then the front of convection approached the western section of the RWP mesonet until 1400 LST (Fig. 4b). One can see rising pressure at the rate of more than 4 hPa in 30 minutes with a strengthening cold pool at the center with a cooling rate of more than 10 ℃ $30min^{-1}$ associated with the main area of the MCS (Fig. 5b). The dry subcloud air was one of the factors that facilitated cold pool consolidation and rapid organization of convection.

It's clearly shown in Figs. 4c and 5c that stronger thunderstorms persisted at 1412 LST with convectively generated cold air. Of particular relevance to this study is the emergence of a convective line near 39.7°N, 115.6°E at the leading edge of the cold outflows (Fig. 5c). This convective line formed from the low-level convergence as the north-to-northeasterly cold outflows met westerly winds to the south, which appeared to help initiate convection cells to the west of the plain line. Shortly after, explosive convection emerged (Fig. 4d) along the convective line (Fig. 5d) as the outflow boundary entered the plain at 1424 LST. However, it is noteworthy that only light precipitation appeared to reach the ground prior to 1430 LST with rainfall rate less than 3mm $30min^{-1}$ (Fig. 2b). The evaporative cooling effect of precipitation particles likely fostered the development of evaporatively cooled air that expanded rapidly over the western mountain region, as mentioned before. Furthermore, the distinct local wind maximum was attributed partly to the venturi effect by canyon. As shown in Fig. 1, there exist many long and narrow valleys at the junction of the southern foothill of Mt. Yan and the eastern foothill of Mt. Taihang. Northwesterly cold air rapidly accelerated and swept across downwind areas after being funneled through canyons and mountain passes (Grubisic et al., 2008; Smith, 1979). It is well known that Santa Ana winds with gusts exceeding 100 $km\,h^{-1}$ is closely connected with the channels over the Sierra Nevada and Transverse Ranges (Guzman-Morales et al., 2016; Prein et al., 2022), destroy crops and greatly enhance the spread of wildfires for centuries (Kelley et al., 2025). In addition, lower surface roughness in the mountainous areas also results in

https://doi.org/10.5194/egusphere-2025-5371
Preprint. Discussion started: 7 November 2025

higher 10-m wind speeds (Barthelmie, 2001; Luu et al., 2023), especially when the dry environment is unfavorable for vegetation growth, while urban buildings increase frictional drag and surface roughness length z_0 values over a city (Oke, 1987).

At this time, a leading stratiform region consisting of several dispersed convective cells, denoted as C2, was located to the north of the mesonet (Fig. 4a). The convection cell near HR maintained and developed rapidly in coverage and intensity from 1400 to 1424 LST (Fig. 4b-d) due to the persistent convergence of low-level southerly flows at the foot of Mt. Yan (Fig. 5b-d). This coincided with a surface cold pool with T_{2m} drops as large as 6°C in 30 minutes. After 1436 LST, it gradually merged with the southern convective segment as mentioned above and strengthened to an intense and well-organized squall line that had a nearly contiguous reflectivity region of 35 dBZ at least 150 km in length (Fig. 4e and f). The southern convective line significantly extended after intersecting with the preexisting convergence zone at the foothills of Mt. Yan (Fig. 5e, f). Apparently, the appearance of a secondary maximum 10 m wind speed area in Fig. 2c coincided with the intensification of the gust front, as evidenced by its increased width and echo intensity. The continuous increasing of rainfall in triangle 1 and 2 (cf. Fig. 2c) resulted in a distinct cold center at the cooling rate of more than 12 °C.

The squall line subsequently developed a larger-scale bow echo (Fujita 1978) and accelerated to the east-southeast as the system became oriented more perpendicular to the mean northwest wind in the middle troposphere (Fig. 4g, h). The QLCS subsequently moved eastward with the leading convective line and a trailing stratiform region during the mature stage (Fig. 4g, h), which are similar to the asymmetric archetype of a squall line found by Johnson and Hamilton (1988) and Zhang et al. (1989). The midlevel rear-inflow jet (RIJ) that feeds into the stratiform region of QLCSs plays an important role in producing the high winds at the surface (Weisman & Davis, 1998; Xu et al.,2024), which has also occurred in the present case, as shown in the next subsection.

https://doi.org/10.5194/egusphere-2025-5371
Preprint. Discussion started: 7 November 2025

4. Vertical Structures of the Gusty Winds

4.1 Horizontal divergence and vertical vorticity analyses

In the preceding section, the synoptic-scale weather system was shown to be favorable for stronger convection with evidently identifiable boundaries of the 30 May 2024. Here, the localized environmental conditions are analyzed for forcing mechanisms supporting the advancing regeneration of convection along the leading line and associated winds. To gain insight into the fine-scale structures of this extreme wind gust event, we calculated the height-time cross sections of horizontal winds and vertical motion from the RWPs during 1300-1530 LST on 30 May 2024. Figure 6 presents the vertical distribution of vertical vorticity (ζ) and horizontal divergence (D) within triangular regions calculated from Equations 1 and 2, together with the evolution of the 95th percentile of the 10-m wind speed. The 95th percentile was selected rather than the maximum value to provide a more robust representation of the overall distribution.

Before the MCS reached Beijing, sustained low-level south-to-southwesterly wind was observed in the lowest 1.5 km layer in the early afternoon of 30 May 2024 from seven RWP stations (not shown), accompanied by weak near-surface convergence in the main plain area (Fig. 6b-d). Especially, more noticeable convergence in the lower to mid-troposphere was detected locally over triangle 3 after 1300 LST (Fig. 6c) by the uplifting along the foothills of Mt. Yan. Divergence below 4 km AMSL in triangle 1 could to a certain extent be influenced by the valley flows at the foot of the Taihang mountains (Fig. 6a). As the main convective element C1 propagated eastward, an evident increase was observed in horizontal convergence in the lowest 2 km AMSL layer along the leading line of the strengthening cold pool after 1342 LST (Fig. 6a, b). The convergence and associated updraft increased in amplitude and deepened rapidly, resulting in the generation of clouds and convective cells along the downshear side of the cold pool that expanded southward and eastward after 1400 LST (see Fig. 4b-d). The presence of divergence aloft above near-surface convergence layers confirmed the development of this deep, organized convection that played an important role in generating precipitation. It created favorable conditions for the evaporative cooling to

https://doi.org/10.5194/egusphere-2025-5371
Preprint. Discussion started: 7 November 2025

accelerate the enhancement of the cool pool. The intense cold pool, in turn, was the primary driver for high winds through the downward momentum transport and pressure gradient forcing.

Of importance to note is the rapid growth of surface-based positive vorticity over triangle 2 coupled with intense convergence across the gust-frontal zone during the passage of the main convective element. A deep layer of cyclonic vorticity was detected in the lower half of the troposphere over triangle 2 with the maximum value of -2.8× 10^{-4} s^{-1} centering near 3 km AMSL at 1436 LST. The strongest surface wind speed at the 95th percentile appeared nearly in phase after the peak of cyclonic vorticity, as also shown in Fig. 6b. These structures are similar to those shown by Zhang (1992), suggesting that the moderate positive ζ was generated through upward vortex stretching ahead of convection, whereas the large negative ζ, likely located behind, resulted from the downward stretching of moderate negative (absolute) ζ. Weisman and Trapp (2003) found that mesoscale vortices may be responsible for the production of damaging straight-line winds by notably modifying the local outflow and determining the location of the wind speed maximum.

The northeastern dispersed convective cores with radar reflectivity more than 35 dBZ were completely separated from the major convective segment to the south and remained closely related to the convergence of southwesterly flows over triangle 3 (Fig. 6c), like the counterpart of the surface streamline shown in Fig. 4. The surface-based convergence strengthened over triangle 3 and 4 after 1400 LST, with divergence above (Fig. 6c, d) in the absence of significant local evaporative cooling. After merging with the main area of convection, which moved across the plain line in the urban region after 1436 LST, a deep layer of convergence and intense upward motion (above 5 km AMSL) over triangles 3 and 4 enhanced the squall line (Fig. 6c, d), leading to heavy rainfall (Fig. 2c). We may speculate that the low-level cyclonic vorticity of 1.8×10^{-4} s^{-1} (i.e., centered at 1-km altitude) after 1436 LST coincided with the development of the area-averaged convergence during the periods, similar to that captured by triangle 2. Moreover, the intersection of two segments formed a pivot point in triangle 3 (Fig. 2f)

https://doi.org/10.5194/egusphere-2025-5371
Preprint. Discussion started: 7 November 2025

for the change in line orientation and marked the area of mesovortices under study. Both the area and intensity of the observed high winds increased remarkably during this hour (Fig. 6c), with the most severe winds over 30 m s^{-1} and significant property damage occurring in the merger region (Fig. 2c). The development of a large, intense MCS resulted from a complex series of processes and mergers of several convective lines and clusters over a relatively short time period, which is also common for warm season MCSs (French and Parker; 2012).

Note that a deep layer of strengthening cyclonic vorticity above 4 km AMSL dominated triangles 3 and 4 after the merger (Fig. 6c, d) and gradually extended downward to an altitude of 3 km, with the center value exceeding 2.8×10^{-4} s^{-1}. This suggests that the mid-level rotation of the frontal vortex played an important role in enhancing the elevated RIJ, similar to the enhancement of near-surface high winds by the low-level rotation. The strongest winds tended to occur on the southwestern side of the mesoscale vortices, where the ambient translational northwesterly flow and the mesoscale vortices' rotational flow were aligned (e.g., Wakimoto et al., 2006; Atkins and St. Laurent, 2009; Xu et al., 2015b). The intensification of the RIJ was likely due to the locally enhanced cold pool from increased rainfall in the merger area (Fig. 2).

Simultaneously, the lower-tropospheric convergence in triangle 1 and 2 started showing a decreasing trend, followed by large negative ζ in descending rear inflows. In addition, the surface wind speed diminished dramatically with significant divergence in the lowest 2-km layer shortly (i.e., between 1500 and 1530 LST) after the passage of the gust front. The changeover to divergence was likely driven by evaporative cooling of raindrops, as evidenced by the emergence of outflows behind the leading convective line, which could also to a certain extent be influenced by downslope flows over the western mountains. One may note the presence of elevated, much weaker convergence centered at 3 km. This could be attributed to the approach of trailing stratiform precipitation (see Figs. 11b and 12e, f), as indicated by Houze et al. (1989) and Zhang and Gao (1989) in their respective observational and modeling studies of squall lines.

https://doi.org/10.5194/egusphere-2025-5371
Preprint. Discussion started: 7 November 2025

4.2 Deformation and frontogenesis analysis

To the forecaster, the most significant aspects of a frontal zone are the cloudiness and convection that are usually associated with it. Horizontal convergence and deformation fields are two key mechanisms that drive frontogenesis by concentrating temperature gradients and enhancing frontal sharpness. Figure 7a shows the evolution of the frontogenesis function and shearing deformation as described in subsection 2.4 and appeared to depict this frontogenesis event in the low-level layer. Both stretching and shearing deformation cause some parts of the air parcel to move towards each other and result in weather fronts. Shearing deformation was positively associated with the air parcel stretching in the southwest/northeast direction and contracting in the southeast/northwest direction. Convection developed along this feature as it moved north and east. Likely aiding the convective development was the strong horizontal convergence and low-level deformation frontogenesis. This conclusion is supported by the fact that the squall line aligned with the long axis of the frontogenesis (Fig. 4e-h).

Triangle 1 and 2 experienced weak frontogeneses in the lowest 1.5 km layer before the arrival of the southeast segment (cf. Fig. 7a, b). As the horizontal convergence increased, frontogenesis was strengthened after 1330 LST up to the middle altitude of 3 km with a peak value of 4.8×10^{-8} K m^{-1} s^{-1} near 1.5 km AMSL at 1424 LST over triangle 1. The convergence contributed to the compression of the temperature gradient and promoted the strong concentrated sloping updraft occurring on the warm side of the region of maximum geostrophic compression of the isotherms. This mesoscale circulation closely resembles the flow in a mesoscale precipitation band analyzed by Emanuel (1985), Bosart and Sanders (1981). Cold outflows associated with evaporatively driven moist downdrafts were evident, with the continuous cooling rate of about 15 K h^{-1} by 1500 LST in triangle 1 and 2 (Fig. 7a, b). By contrast, a sharp drop of area-averaged θ_e in triangle 3 was generated by significant rainfall which took place in the merger stage (Fig. 7c). The warming pattern was observed in triangle 2 with rising θ_e, which was possibly attributed to the dry subsidence warming associated with the descending RIJ at the back edge of the precipitation region.

https://doi.org/10.5194/egusphere-2025-5371
Preprint. Discussion started: 7 November 2025

4.3 Vertical momentum transport

Apparently, the passage of the wind gust resulted in significant alterations to the vertical profiles and intensity of the above fields. Specifically, weaker southwest-to-westerly flows with wind speed less than 8 m s^{-1} up to 1.5 km AMSL were detected by the RWP at HD prior to the arrival of the gust front (Fig. 8a) from the height-time cross section of horizontal winds. Meanwhile, the northwesterly jet exceeding 15 m s^{-1} controlled the higher altitude above 3 km AMSL. Evidently, such an intense gust front was related to the critical influence that substantial vertical wind shear exerts on convection. Then, sharp wind directional shifts to northwesterly happened with increasing 10 m wind speeds from less than 5 m s^{-1} to more than 10 m s^{-1} in the lowest 1-km layer at 1436 LST. The intense northwest-to-northerly winds with strong descending motion coincided with the occurrences of light rainfall with the total accumulation of about 5 mm (Fig. 8a), pronounced surface temperature drops and pressure rising (Fig 8b). The effect of light precipitation on the radar measurement was neglected because the fluctuating component of the horizontal velocity was much larger in magnitude. The precipitation was just concentrated near 1442 LST and decreased rapidly to less than 1 mm per 6 minutes shortly thereafter. Given that the weak precipitation ended by 1500 LST, the vertical velocity associated with the squall line (i.e., -8 m s^{-1} shown in Fig. 8c) represented the intensity of evaporatively induced downdrafts rather than the falling speed of the raindrops.

Previous studies have used the horizontal momentum budget equation to diagnose the contribution of each term in momentum transport within MCSs, mostly in modeling studies (Mahoney & Lackmann, 2011; Mahoney et al., 2009). To investigate the roles of internal circulations of the MCS in producing the present wind gust event, the vertical momentum transport of zonal wind, $-w\partial u/\partial z$ was estimated. Figure 8c shows enhanced near-surface positive tendencies of the vertical advection at HD below 1 km AMSL ahead the gust front. In response to the forcing of the QLCS, the elevated RIJ occurring in the western portion of the mesovortex after 1436 LST corresponded well to the vertical structure observed by the RWP mesonet in subsection 4.1. The RIJ was

https://doi.org/10.5194/egusphere-2025-5371
Preprint. Discussion started: 7 November 2025

also amplified by developing downdrafts behind the gust front with the maximum value more than -8 m s^{-1} near 1500 LST. The accelerated downward transport of high momentum associated with the RIJ produced intensified high winds of over 25 m s^{-1} below 1 km AGL (Fig. 8a) at 1512 LST. Thus, we may state that the above evidence is further indicative of the important roles of downward momentum transport with the descending rear inflows in generating the damaging wind event under study.

4.4 Turbulent kinetic energy transfer

As the well-sustained mesoscale convection created a favorable dynamic environment for the evolution of small-scale turbulent processes, the interaction between the organized squall system (and its embedded mesovortex and rear-inflow jet) and the ambient flow laid the foundation for the subsequent intensification of turbulent energy transfer, which is essential for the evolution of severe convective gust and related convective activities (Adler and Kalthoff, 2014; Dai et al., 2014; Dodson and Griswold, 2021; Su et al., 2023). Understanding mechanisms of the turbulent kinetic energy (TKE) transferring in the PBL between the surface and atmosphere is crucial for turbulence parameterization in numerical models, especially for extreme wind events (Lyu et al., 2023; Monahan et al., 2015; Powell et al., 2003).

In contrast to the Monin-Obukhov similarity theory that TKE transfers from larger to smaller eddies until it is dissipated at the smallest scales (Kolmogorov, 1941; Monin & Obukhov, 1954), many studies discovered the phenomenon of inverse energy cascades (IEC) in a totally different way (Byrne & Zhang, 2013; Kraichnan, 1967; Tang et al., 2015). Despite these advances in theoretical and numerical studies, observational support for IEC in the atmosphere remains insufficient (Shao et al., 2023a, Shao et al., 2023b). This study further examined the direction of the energy cascade associated with wind gusts using three-dimensional ultrasonic anemometers at seven heights, denoted as z_1 to z_7, on the meteorological tower in Beijing. According to Eq. (11), the energy flux can only be obtained at six heights (from z_1 to z_6) by the differences of vertical velocity (w_2-w_1, w_3-w_2, ..., w_7-w_6) between two adjacent heights. Therefore, there were six samples to identify IEC for every moment.

https://doi.org/10.5194/egusphere-2025-5371
Preprint. Discussion started: 7 November 2025

The frequency of IEC during a period was evaluated as the ratio of the number of IEC grids to the total number of samples. In this way, we got height-resolved occurrence frequency of IEC for the study period in Fig. 9a. It is shown that IEC is a more prevalent phenomenon within the near-surface wind field. Notably, the frequency and intensity of IEC increased significantly when near-surface wind speeds exceeded 10 m s^{-1}. The frequency of IEC reaches up to 50% after 1436 LST, indicating that strong winds are contributed to IEC. The results in Fig. 9b and c revealed that the power spectral density (PSD) was higher after 1436 LST in the lower-frequency area, especially for the *u* and *v* directions, which confirmed the activity of turbulent kinetic energy from smaller to larger eddies.

These features were similar to those proposed by the observational analyses in 2D turbulence (Shao et al., 2022; Zhou et al., 2025), which suggested that the reduction of surface drag coefficient under robust weather systems impedes the dissipation of energy throughout the boundary layer. The accumulation of wind energy is a crucial driver of IEC, promoting the formation of a giant, coherent vortex. The amplification of large-scale eddies transfer momentum to the surface more efficiently and enhance wind gusts as a form of positive feedback. corresponding with stronger low-level wind speeds and gusts. These findings provided favorable evidence for the unique features of 2D turbulence in high wind conditions. In the future, the exploration of mechanisms driving the formation of IEC and its association with various weather phenomena are warranted.

5. Concluding remarks and summary

The complex evolution of convective systems crossing mountainous terrain, and their associated damaging surface winds, represents a substantial forecasting challenge. This study examines a convectively generated gust wind event, produced by a Quasi-Linear Convective System (QLCS) that occurred in Beijing during the early afternoon of 30 May 2024. The intricate topography of Beijing added inherent complexity to the convective organization during the downhill thunderstorm process, which led to the development of the extreme wind gust. To document the development and evolution of

https://doi.org/10.5194/egusphere-2025-5371
Preprint. Discussion started: 7 November 2025

the convective event, we explored the dynamical characteristics of the multiscale processes by utilizing a high-resolution mesonet comprised of seven radar wind profilers (RWPs), a meteorological tower, automated surface stations (AWSs), and radar and satellite data. A conceptual model for the dynamical structure for this extreme wind gust event in Beijing is given in Fig. 10.

Large-scale meteorological analyses show that the deep, well-mixed boundary layer with very steep lower-tropospheric lapse rates and conditional instability provided the favorable background for consolidating the dispersed multicell thunderstorm. The northern convection portion maintained and developed rapidly due to the convergence of southerly winds along the southern slopes of Mt. Yan. Meanwhile, the convergence line formed at the boundary of convectively generated cold outflows mostly associated with the southern portion. During the downhill process, the environmental southerly winds in the near-surface layer allowed for very efficient storm-relative inflow of very unstable air that supported the continued regeneration of strong convection along the advancing cold pool, where a very large area of nearly contiguous radar reflectivity echoes greater than 45 dBZ was concentrated over the foot of western mountains. After reaching the plain, two convective segments subsequently merged into a well-organized squall system and moved perpendicular to the mean deep-layer wind/shear and developed a larger-scale bow-echo structure.

Triangular calculations of the vertical vorticity and horizontal divergence from the RWP mesonet qualitatively indicate the contribution of dynamic process to the high winds as the convection entered the mesonet. The presence of pronounced convergence from the PBL in updrafts led to the rapid intensification of surface based cyclonic vorticity through vertical stretching during the early stages. The generation of the extreme winds was enhanced by the evaporative cooling effect through the downward momentum transport and pressure gradient forcing. In the merger stage, a midlevel layer of intense cyclonic vorticity favored the RIJ behind the precipitation area by the superposition of ambient flow with the rotational flow on on the west side of vortex. A calculation of the meridional momentum budget further confirmed the importance of

https://doi.org/10.5194/egusphere-2025-5371
Preprint. Discussion started: 7 November 2025

the downward transport of horizontal momentum in accelerating lower-level flows in the descending RIJ.

The emergence of pronounced low-level frontogenesis, coupled with significant shearing deformation, created a highly favorable synoptic-scale environment for the sustained convection. These processes provided persistent forcing for ascent and low-level convergence, which continuously supplied moisture and instability, thereby promoting the organization and maintenance of the circulation. By further examining the property of turbulent kinetic energy transferring derived from three-dimensional ultrasonic anemometers on the meteorological tower, it was discovered that the frequency and intensity of inverse energy cascades increased significantly when near-surface high winds occurred. These results bridge the gap between meso- and small-scale physical processes in the lower troposphere and the large-scale weather system, which potentially consolidate our understanding of dynamics and their roles in the evolution of convection.

The novelty of this study lies at the explicit multiscale processes governing the generation of an extreme gusty wind event, which is seldom revealed in previous studies using high-resolution vertical observation derived from a high-density RWP mesonet. This mesonet have provided valuable insights into capturing the vertical structures of QLCS and validating the numerical simulation results of other studies. More importantly, the mechanisms of convective evolution and its interactions with complex terrain in different stages has been elaborated, which are favorable for the characterization of such extreme wind events. These findings have important implications for improving parameterizations of extreme weather prediction and enhancing the accuracy and reliability of wind gust forecasting. However, it should be mentioned that RWPs have limited capability in detecting near-surface wind fields and thermal parameters. It's beneficial to applying wind lidars and microwave radiometers for filling the observational gaps and exploring thermodynamic drivers of extreme wind gust events.

https://doi.org/10.5194/egusphere-2025-5371
Preprint. Discussion started: 7 November 2025

Author contributions

JG designed the research framework and conceptualized this study; XG and JG conducted the experiment and drafted the initial manuscript; YS and FH helped the data collection from the meteorological tower and carried out data quality control; NL, ZZ, PY, SJ, LZ and TC participated in result interpretation and discussions; All authors contributed to the revision of the manuscript.

Competing interests

The contact author has declared that there are no competing interests for all authors.

Financial support

This manuscript was supported by the National Natural Science Foundation of China under grant 42325501, Key Laboratory of South China Sea Meteorological Disaster Prevention and Mitigation of Hainan Province under grant SCSF202409, and the National Key Research and Development Program by the Ministry of Science and Technology in China under grant 2024YFC3013001.

Data availability

We are grateful to ECMWF for providing ERA5 hourly data by Copernicus Climate Change Service (C3S) Climate Data Store (CDS), which are available at https://doi.org/10.24381/cds.bd0915c6 (Hersbach et al., 2023). The meteorological measurements of automatic weather stations are obtained from the National Meteorological Information Center of China Meteorological Administration (https://data.cma.cn) via registration.

https://doi.org/10.5194/egusphere-2025-5371
Preprint. Discussion started: 7 November 2025

References

Abulikemu, A., Wang, Y., Gao, R., Wang, Y., & Xu, X. (2019). A numerical study of convection initiation associated with a gust front in Bohai Bay Region, North China. J. Geophys. Res. Atmos., 124, 13843 – 13860. https://doi.org/10.1029/2019JD030883

Adams-Selin, R. D., van den Heever, S. C., & Johnson, R. H. (2013). Impact of Graupel parameterization schemes on idealized bow echo simulations. Mon. Wea. Rev., 141, 1241–1262. https://doi.org/10.1175/MWR-D-12-00064.1

Adler, B. & Kalthoff, N. (2014). Multi-scale transport processes observed in the boundary layer over a mountainous island. Bound.-Lay. Meteorol., 153, 515–537. https://doi.org/10.1007/s10546-014-9957-8

Atkins, N. T., Bouchard, C. S., Przybylinski, R. W., Trapp, R. J., & Schmocker, G. (2005). Damaging surface wind mechanisms within the 10 June 2003 Saint Louis bow echo during BAMEX. Mon. Wea. Rev., 133, 2275 – 2296. https://doi.org/10.1175/MWR2973.1

Atkins, N. T., & Laurent, M. St. (2009). Bow echo mesovortices. Part I: Processes that influence their damaging potential. Mon. Wea. Rev., 137, 1497 – 1513. https://doi.org/10.1175/2008MWR2649.1

Azorin-Molina, C., Guijarro, J.-A., Mcvicar, T. R., Vicente-Serrano, S. M., Chen, D., Jerez, S., & Espírito-Santo, F. (2016). Trends of daily peak wind gusts in Spain and Portugal, 1961–2014. Journal of Geophysical Research: Atmospheres, 121(3), 1059–1078. https://doi.org/10.1002/2015JD024485

Barthelmie, R.J. (2001), Evaluating the impact of wind induced roughness change and tidal range on extrapolation of offshore vertical wind speed profiles. Wind Energ., 4: 99-105. https://doi.org/10.1002/we.45

Bélair, F., Dyer-Hawes, Q. & Romanic, D. (2025). The Dynamics of the Urban

https://doi.org/10.5194/egusphere-2025-5371
Preprint. Discussion started: 7 November 2025

Boundary Layer Before and During a Severe Thunderstorm Outflow Over Downtown Montr é al. Boundary-Layer Meteorol., 191, 6. https://doi.org/10.1007/s10546-024-00896-4

Bellamy, J. C. (1949). Objective calculations of divergence, vertical velocity and vorticity. Bulletin of the American Meteorological Society, 30(2), 45–49. https://doi.org/10.1175/1520-0477-30.2.45

Bentley, M. L., & Sparks, J. M. (2003). A 15 yr climatology of derecho-producing mesoscale convective systems over the central and eastern United States. Climate Res., 24, 129—139.

Bentley, M. L., & Mote, T. L. (1998). A Climatology of Derecho-Producing Mesoscale Convective Systems in the Central and Eastern United States, 1986–95. Part I: Temporal and Spatial Distribution. Bull. Amer. Meteor. Soc., 79, 2527–2540. https://doi.org/10.1175/1520-0477(1998)079<2527:ACODPM>2.0.CO;2

Bessho, K., Date, K., Hayashi, M., Ikeda, A., Imai, T., Inoue, H., et al. (2016). An introduction to Himawari-8/9 — Japan's new-generation geostationary meteorological satellites. Journal of the Meteorological Society of Japan Series II, 94(2), 151–183. https://doi.org/10.2151/jmsj.2016-009

Bluestein, H. B. (1986). Fronts and Jet Streaks: A Theoretical Perspective. In P. S. Ray (Ed.), Mesoscale meteorology and forecasting (pp. 173 – 215). American Meteorological Society. https://doi.org/10.1007/978-1-935704-20-1_9

Bony, S., & Stevens, B. (2019). Measuring area-averaged vertical motions with dropsondes. J. Atmos. Sci., 76, 767-783. https://doi.org/10.1175/JAS-D-18-0141.1

Bosart, L. R., & Sanders, F. (1981). The Johnstown flood of July 1977: A long-lived convective system. J. Atmos. Sci., 38, 1616−1642, https://doi.org/10.1175/1520-0469(1981)038<1616:TJFOJA>2.0.CO;2

Burghardt, B. J., Evans, C., & Roebber, P. J., (2014). Assessing the predictability of

https://doi.org/10.5194/egusphere-2025-5371
Preprint. Discussion started: 7 November 2025

convection initiation in the high plains using an object-based approach. Weather and Forecasting, 29(2), 403–418. https://doi.org/10.1175/WAF-D-13-00089.1

Brandes, E. A., & Ziegler, C. L. (1993). Mesoscale downdraft influences on vertical vorticity in a mature mesoscale convective system. Mon. Wea. Rev., 121, 1337-1353. https://doi.org/10.1175/1520-0493(1993)121<1337:MDIOVV>2.0.CO;2

Byrne, D., & Zhang, J. A. (2013). Height-dependent transition from 3-D to 2-D turbulence in the hurricane boundary layer. Geophysical Research Letters, 40(7), 1439–1442. https://doi.org/10.1002/grl.50335

Chen, D., Guo, J., Yao, D., Lin, Y., Zhao, C., Min, M., et al. (2019). Mesoscale convective systems in the Asian monsoon region from Advanced Himawari Imager: Algorithms and preliminary results. Journal of Geophysical Research: Atmospheres, 124, 2210–2234. https://doi.org/10.1029/2018JD029707

Chen, M., Wang, Y., Gao, F., & Xiao, X. (2012). Diurnal variations in convective storm activity over contiguous North China during the warm season based on radar mosaic climatology, J. Geophys. Res.-Atmos., 117, D20115. https://doi.org/10.1029/2012JD018158.

Chen, M., Wang, Y., Gao, F., & Xiao, X. (2014). Diurnal evolution and distribution of warm - season convective storms in different prevailing wind regimes over contiguous North China, J. Geophys. Res.-Atmos., 119, 2742–2763.

Chen, T., Guo, J., Guo, X., Zhang, Y., Xu, H., & Zhang, D.-L. (2024). On the multiscale processes leading to an extreme gust wind event in East China: Insights from radar wind profiler mesonet observations. Journal of Geophysical Research: Atmospheres, 129, e2024JD041484. https://doi.org/10.1029/2024JD041484

Coniglio, M. C., Corfidi, S. F., & Kain, J. S. (2011). Environment and early evolution of the 8 May 2009 derecho-producing convective system. Mon. Wea. Rev., 139, 1083–1102. https://doi.org/10.1175/2010MWR3413.1

Da, C. (2015). Preliminary assessment of the Advanced Himawari Imager (AHI) measurement onboard Himawari-8 geostationary satellite. Remote Sensing Letters, 6, 637–646. https://doi.org/10.1080/2150704x.2015.1066522

https://doi.org/10.5194/egusphere-2025-5371
Preprint. Discussion started: 7 November 2025

708 Dai, C., Wang, Q., Kalogiros, J. A., Lenschow, D. H., Gao, Z., & Zhou, M. (2014)
709 Determining boundary-layer height from aircraft measurements. Bound.-Lay.
710 Meteorol., 152, 277–302. https://doi.org/10.1007/s10546-014-9929-z
711 Davis, C. A., & Trier, S. B. (2007). Mesoscale convective vortices observed during
712 BAMEX. Part I: Kinematic and thermodynamic structure. Monthly Weather
713 Review, 135(6), 2029–2049. https://doi.org/10.1175/MWR3398.1
714 Dodson, D. S. & Small Griswold, J. D. (2021). Turbulent and boundary layer
715 characteristics during VOCALS-REx. Atmos. Chem. Phys., 21, 1937–1961.
716 https://doi.org/10.5194/acp-21-1937-2021
717 Emanuel, K. A. (1985). Frontal Circulations in the Presence of Small Moist Symmetric
718 Stability. J. Atmos. Sci., 42, 1062–1071. https://doi.org/10.1175/1520-
719 0469(1985)042<1062:FCITPO>2.0.CO;2
720 Evans, C., Weisman, M. L., & Bosart, L. F. (2014). Development of an intense, warm-
721 core mesoscale vortex associated with the 8 May 2009 "super derecho"
722 convective event. J. Atmos. Sci., 71, 1218–1240. https://doi.org/10.1175/JAS-D-
723 13-0167.1
724 Fiori, E., Parodi, A., & Siccardi, F. (2011). Uncertainty in prediction of deep moist
725 convective processes: Turbulence parameterizations, microphysics and grid-scale
726 effects. Atmospheric Research, 100(4), 447 – 456.
727 https://doi.org/10.1016/j.atmosres.2010.10.003
728 Fovell, R. G. (2002). Upstream influence of numerically simulated squall-line storms.
729 Quart. J. Roy. Meteor. Soc., 128, 893 – 912.
730 https://doi.org/10.1256/0035900021643737
731 Fovell, R. G., and Y. Cao, (2014). Wind and gust forecasting in complex terrain. 15th
732 WRF Users ' Workshop, Boulder, CO, NCAR,
733 5A.2, http://www2.mmm.ucar.edu/wrf/users/workshops/WS2014/ppts/5A.2.pdf.
734 French, A. J., & Parker, M. D. (2012). Observations of mergers between squall lines
735 and isolated supercell thunderstorms. Wea. Forecasting, 27, 255 – 278.

https://doi.org/10.5194/egusphere-2025-5371
Preprint. Discussion started: 7 November 2025

https://doi.org/10.1175/WAF-D-11-00058.1

French, A. J., & Parker, M. D. (2014). Numerical simulations of bow echo formation following a squall line–supercell merger. Mon. Wea. Rev., 142, 4791–4822. https://doi.org/10.1175/MWR-D-13-00356.1

Fujita, T. T. (1978). Manual of downburst identification for Project NIMROD. Satellite and Mesometeorology Research Paper 156, 111 pp.. https://ntrs.nasa.gov/citations/19780022828

Goyette, S., Brasseur, O., & Beniston, M. (2003). Application of a new wind gust parameterization: Multiscale case studies performed with the Canadian regional climate model. Journal of Geophysical Research: Atmospheres, 108, 4374. doi:10.1029/2002JD002646, D13.

Guo, J., Zhang, J., Yang, K., Liao, H., Zhang, S., Huang, K., Lv, Y., Shao, J., Yu, T., Tong, B., Li, J., Su, T., Yim, S. H. L., Stoffelen, A., Zhai, P., & Xu, X. (2021). Investigation of near-global daytime boundary layer height using high-resolution radiosondes: First results and comparison with ERA-5, MERRA-2, JRA-55, and NCEP-2 reanalyses. Atmos. Chem. Phys., 21, 17079 – 17097. https://doi.org/10.5194/acp-21-17079-2021

Guo, X., Guo, J., Zhang, D-L., & Yun, Y. (2023). Vertical divergence profiles as detected by two wind profiler mesonets over East China: implications for nowcasting convective storms, Q. J. R. Meteorol. Soc., 149(754), 1629-1649. doi:10.1002/qj.4474

Guo, X., Guo, J., Chen, T., Li, N., Zhang, F., & Sun, Y. (2024). Revisiting the evolution of downhill thunderstorms over Beijing: a new perspective from a radar wind profiler mesonet, Atmos. Chem. Phys., 24, 8067 – 8083. https://doi.org/10.5194/acp-24-8067-2024

Guzman-Morales, J., A. Gershunov, J. Theiss, H. Li, and D. Cayan (2016), Santa Ana Winds of Southern California: Their climatology, extremes, and behavior spanning six and a half decades, Geophys. Res. Lett., 43, 2827 – 2834,

https://doi.org/10.5194/egusphere-2025-5371
Preprint. Discussion started: 7 November 2025

https://doi.org/10.1002/2016GL067887

Grim, J. A., Rauber, R. M., McFarquhar, G. M., Jewett, B. F., & Jorgensen, D. P. (2009). Development and forcing of the rear inflow jet in a rapidly developing and decaying squall line during BAMEX. Monthly Weather Review, 137(4), 1206–1229. https://doi.org/10.1175/2008mwr2503.1

Grubišić, Vanda and Doyle, James D. and Kuettner, Joachim and Mobbs, Stephen and Smith, Ronald B. and Whiteman, C. David and Dirks, Richard and Czyzyk, Stanley and Cohn, Stephen A. and Vosper, Simon and Weissmann, Martin and Haimov, Samuel and De Wekker, Stephan F.J. and Pan, Laura L. and Chow, Fotini Katopodes (2008) The terrain-induced rotor experiment: A field campaign overview including observational highlights. Bulletin of the American Meteorological Society, pp. 1-21. American Meteorological Society. doi: 10.1175/2008BAMS2487.1.

Hadavi, M., & Romanic, D. (2024). Atmospheric conditions conducive to thunderstorms with downbursts in Canada and a downburst precursor parameter. Atmos. Res., 305(107), 428. https://doi.org/10.1016/j.atmosres.2024.107428

Han, B., Du, Y., Wu, C., & Liu, X. (2021). Microphysical characteristics of the coexisting frontal and warm-sector heavy rainfall in South China. Journal of Geophysical Research: Atmospheres, 126, e2021JD035446. https://doi.org/10.1029/2021JD035446

Harris, A. R., & Kahl, J. D. W. (2017). Gust factors: Meteorologically stratified climatology, data artifacts, and utility in forecasting peak gusts. Journal of Applied Meteorology and Climatology, 56(12), 3151–3166. https://doi.org/10.1175/jamc-d-17-0133.1

Hirt, M., & Craig, G. C. (2021). A cold pool perturbation scheme to improve convective initiation in convection-permitting models. Quarterly Journal of the Royal Meteorological Society, 147(737), 2429–2447. https://doi.org/10.1002/qj.4032

Johns, R. H., & Hirt, W. D. (1987). Derechos: Widespread convectively induced

https://doi.org/10.5194/egusphere-2025-5371
Preprint. Discussion started: 7 November 2025

windstorms. Wea. Forecasting, 2, 32–49. https://doi.org/10.1175/1520-0434(1987)002<0032:DWCIW>2.0.CO;2

Kahl, J. D. W. (2020). Forecasting peak wind gusts using meteorologically stratified gust factors and MOS guidance. Weather and Forecasting, 35(3), 1129–1143. https://doi.org/10.1175/waf-d-20-0045.1

Kelley, D. I., Burton, C., Di Giuseppe, F., Jones, M. W., Barbosa, M. L. F., Brambleby, E., McNorton, J. R., Liu, Z., Bradley, A. S. I., Blackford, K., Burke, E., Ciavarella, A., Di Tomaso, E., Eden, J., Ferreira, I. J. M., Fiedler, L., Hartley, A. J., Keeping, T. R., Lampe, S., Lombardi, A., Mataveli, G., Qu, Y., Silva, P. S., Spuler, F. R., Steinmann, C. B., Torres-Vázquez, M. Á., Veiga, R., van Wees, D., Wessel, J. B., Wright, E., Bilbao, B., Bourbonnais, M., Gao, C., Di Bella, C. M., Dintwe, K., Donovan, V. M., Harris, S., Kukavskaya, E. A., N'Dri, A. B., Santín, C., Selaya, G., Sjöström, J., Abatzoglou, J. T., Andela, N., Carmenta, R., Chuvieco, E., Giglio, L., Hamilton, D. S., Hantson, S., Meier, S., Parrington, M., Sadegh, M., San-Miguel-Ayanz, J., Sedano, F., Turco, M., van der Werf, G. R., Veraverbeke, S., Anderson, L. O., Clarke, H., Fernandes, P. M., and Kolden, C. A.: State of Wildfires 2024 – 2025, Earth Syst. Sci. Data, 17, 5377 – 5488, https://doi.org/10.5194/essd-17-5377-2025, 2025.

Kolmogorov, A. N. (1941). The local structure of turbulence in incompressible viscous fluid for very large Reynolds numbers. Doklady Akademii Nauk SSSR, 30, 299–303.

Kraichnan, R. H. (1967). Inertial ranges in two-dimensional turbulence. The Physics of Fluids, 10(7), 1417–1423. https://doi.org/10.1063/1.1762301

Lafore, J., & Moncrieff, M. W. (1989). A numerical investigation of the organization and interaction of the convective and stratiform regions of tropical squall lines. Journal of the Atmospheric Sciences, 46(4), 521–544. https://doi.org/10.1175/1520-0469(1989)046<0521:ANIOTO>2.0.CO;2

Lenschow, D. H., Savic-Jovcic, V., & Stevens, B. (2007). Divergence and vorticity from aircraft air motion measurements. J. Atmos. Oceanic Technol., 24, 2062–

https://doi.org/10.5194/egusphere-2025-5371
Preprint. Discussion started: 7 November 2025

2072, https://doi.org/10.1175/2007JTECHA940.1

Letson, F., S. C. Pryor, R. J. Barthelmie, and W. Hu (2018). Observed gust wind speeds in the coterminous United States, and their relationship to local and regional drivers. J. Wind Eng. Ind. Aerodyn., 173, 199–209, https://doi.org/10.1016/j.jweia.2017.12.008.

Li, H., Cui, X., & Zhang, D. L. (2017). On the initiation of an isolated heavy-rain-producing storm near the central urban area of Beijing metropolitan region, Mon. Weather Rev., 145, 181–197. https://doi.org/10.1175/MWR-D-16-0115.1

Liu, B., Guo, J., Gong, W., Shi, L., Zhang, Y., & Ma, Y. (2020). Characteristics and performance of wind profiles as observed by the radar wind profiler network of China. Atmospheric Measurement Techniques, 13(8), 4589–4600. https://doi.org/10.5194/amt-13-4589-2020

Liu, Q., Xu, X., Zhao, K., & Zhou, A. (2023). A merger-formation bow echo caused by low-level mesovortex in South China. Journal of Geophysical Research: Atmospheres, 128, e2022JD037954. https://doi.org/10.1029/2022JD037954

Luchetti, N. T., Friedrich, K., Rodell, C. E., & Lundquist, J. K. (2020). Characterizing thunderstorm gust fronts near complex terrain. Monthly Weather Review, 148(8), 3267–3286. https://doi.org/10.1175/mwr-d-19-0316.1

Luu, L. N., van Meijgaard, E., Philip, S. Y., Kew, S. F., de Baar, J. H. S., & Stepek, A. (2023). Impact of surface roughness changes on surface wind speed over western Europe: A study with the regional climate model RACMO. Journal of Geophysical Research: Atmospheres, 128, e2022JD038426. https://doi.org/10.1029/2022JD038426

Lyu, M., Potter, H., Collins, C. O., Yang, X., & Wang, X. (2023). The impacts of gustiness on the evolution of surface gravity waves. Geophysical Research Letters, 50(12). https://doi.org/10.1029/2023gl104085

Mahoney, K. M., & Lackmann, G. M. (2011). The sensitivity of momentum transport and severe surface winds to environmental moisture in idealized simulations of a mesoscale convective system. Monthly Weather Review, 139(5), 1352–1369.

https://doi.org/10.5194/egusphere-2025-5371
Preprint. Discussion started: 7 November 2025

https://doi.org/10.1175/2010mwr3468.1

Mahoney, K. M., Lackmann, G. M., & Parker, M. D. (2009). The role of momentum transport in the motion of a quasi-idealized mesoscale convective system. Monthly Weather Review, 137(10), 3316–3338. https://doi.org/10.1175/2009mwr2895.1

Marino, R., Pouquet, A., & Rosenberg, D. (2015). Resolving the paradox of oceanic large-scale balance and small-scale mixing. Physical Review Letters, 114(11), 114504. https://doi.org/10.1103/physrevlett.114.114504

Meng, Z., Zhang, F., Markowski, P., Wu, D., & Zhao, K. (2012). A modeling study on the development of a bowing structure and associated rear inflow within a squall line over South China. J. Atmos. Sci., 69, 1182–1207, https://doi.org/10.1175/JAS-D-11-0121.1

Miller, J. E. (1948). ON THE CONCEPT OF FRONTOGENESIS. J. Atmos. Sci., 5, 169–171. https://doi.org/10.1175/1520-0469(1948)005<0169:OTCOF>2.0.CO;2

Monahan, A. H., Rees, T., He, Y., & McFarlane, N. (2015). Multiple regimes of wind, stratification, and turbulence in the stable boundary layer. Journal of the Atmospheric Sciences, 72(8), 3178–3198. https://doi.org/10.1175/jas-d-14-0311.1

Monin, A. S., & Obukhov, A. M. (1954). Basic laws of turbulent mixing in the surface layer of the atmosphere. Tr. Akad. Nauk SSSR Geophiz. Inst., 24, 163.

Nitta, T., & Esbensen, S. (1974). Heat and moisture budget analyses using BOMEX data. Mon. Wea. Rev., 102, 17-28. https://doi.org/10.1175/1520-0493(1974)102,0017:HAMBAU.2.0.CO;2

Oke, T., 1987: Boundary Layer Climates. Academic Press, 345 pp.

Pandya, R. E., & Durran, D. R. (1996). The influence of convectively generated thermal forcing on the mesoscale circulation around squall lines. J. Atmos. Sci., 53, 2924–2951. https://doi.org/10.1175/1520-0469(1996)053<2924:TIOCGT>2.0.CO;2

Peterson, T. C., Karl, T. R., Kossin, J. P., Kunkel, K. E., Lawrimore, J. H., Mcmahon, J. R., et al., (2014). Changes in weather and climate extremes: State of knowledge relevant to air and water quality in the United States. Journal of the Air and Waste

https://doi.org/10.5194/egusphere-2025-5371
Preprint. Discussion started: 7 November 2025

879 Management Association, 64(2), 184–197.
880 https://doi.org/10.1080/10962247.2013.851044
881 Powell, M. D., Vickery, P. J., & Reinhold, T. A. (2003). Reduced drag coefficient for
882 high wind speeds in tropical cyclones. Nature, 422(6929), 279–283.
883 https://doi.org/10.1038/nature01481
884 Prein, A. F., Coen, J., & Jaye, A. (2022). The character and changing frequency of
885 extreme California fire weather. Journal of Geophysical Research: Atmospheres,
886 127, e2021JD035350. https://doi.org/10.1029/2021JD035350
887 Pryor, S. C., & Barthelmie, R. J. (2010). Climate change impacts on wind energy: A
888 review. Renewable and Sustainable Energy Reviews, 14(1), 430–437.
889 https://doi.org/10.1016/j.rser.2009.07.028
890 Pryor, S. C., & Barthelmie, R. J. (2011). Assessing climate change impacts on the near-
891 term stability of the wind energy resource over the USA. Climate Dynamics, 108,
892 8167–8171. https://doi.org/10.1007/s00382-010-0955-3
893 Pryor, S. C., & Barthelmie, R. J. (2021). A global assessment of extreme wind speeds
894 for wind energy applications. Nature Energy, 6(3), 268–276.
895 https://doi.org/10.1038/s41560-020-00773-7
896 Pryor, S. C., Barthelmie, R. J., & Schoof, J. T. (2012). Past and future wind climates
897 over the contiguous USA based on the North American Regional Climate Change
898 Assessment Program model suite. Journal of Geophysical Research, 117(D19),
899 D19119. https://doi.org/10.1029/2012JD017449
900 Romanic, D., Chowdhury, J., Chowdhury, J., & Hangan, H. (2020). Investigation of
901 the transient nature of thunderstorm winds from Europe, the united states, and
902 Australia using a new method for detection of changepoints in wind speed records.
903 Mon. Wea. Rev., 148(9), 3747–3771. https://doi.org/10.1175/MWR-D-19-0312.1
904 Shao, X., Zhang, N., Peng, Z., Zhao, K., Luo, Y., & Song, X. (2022). Observed surface
905 drag coefficient under high wind speed conditions and the relationship with
906 coherent structures. Journal of Geophysical Research: Atmospheres, 127(3).
907 https://doi.org/10.1029/2021jd035301

https://doi.org/10.5194/egusphere-2025-5371
Preprint. Discussion started: 7 November 2025

908 Shao, X., Zhang, N., & Tang, J. (2023a). A physical model for the observed inverse
909 energy cascade in typhoon boundary layers. Geophysical Research Letters, 50(18).
910 https://doi.org/10.1029/2023gl105546
911 Shao, X., Zhang, N., & Tang, J. (2023b). The impact of observed drag reduction over
912 land on typhoon forecasting. Journal of Geophysical Research: Atmospheres,
913 128(17). https://doi.org/10.1029/2022jd038278
914 Shapiro, A., Potvin, C. K., & Jidong, G. (2009). Use of a vertical vorticity equation in
915 variational dual-Doppler wind analysis. J. Atmos. Oceanic Technol., 26, 2089–
916 2106.
917 Shi, Y., & Hu, F. (2020). Ramp-like PM2.5 accumulation process and Z-less similarity
918 in the stable boundary layer. Geophysical Research Letters, 47(3),
919 e2019GL086530. https://doi.org/10.1029/2019gl086530
920 Shi, Y., Hu, F., Xiao, Z. S., Fan, G. Q., & Zhang, Z. (2020). Comparison of four
921 different types of planetary boundary layer heights during a haze episode in
922 Beijing. Science of the Total Environment, 711, 134928.
923 https://doi.org/10.1016/j.scitotenv.2019.134928
924 Smith, R. B. The influence of mountains on the atmosphere. Advances in Geophysics,
925 Academic Press, 1979, 21: 87-230, https://doi.org/10.1016/S0065-
926 2687(08)60262-9
927 Su, T. N., Li, Z. Q., & Zheng, Y. T. (2023). Cloud-Surface Coupling Alters the Morning
928 Transition from Stable to Unstable Boundary Layer. Geophys. Res. Lett., 50,
929 e2022GL102256. https://doi.org/10.1029/2022gl102256
930 Tang, J., Byrne, D., Zhang, J. A., Wang, Y., Lei, X.-T., Wu, D., et al. (2015). Horizontal
931 transition of turbulent cascade in the near-surface layer of tropical cyclones.
932 Journal of the Atmospheric Sciences, 72(12), 4915 – 4925.
933 https://doi.org/10.1175/jas-d-14-0373.1
934 Taszarek, M., Pilguj, N., Orlikowski, J., Surowiecki, A., Walczakiewicz, S., Pilorz, W.,
935 et al., (2019). Derecho evolving from a mesocyclone—A study of 11 August 2017
936 severe weather outbreak in Poland: Event analysis and high-resolution simulation.

https://doi.org/10.5194/egusphere-2025-5371
Preprint. Discussion started: 7 November 2025

Monthly Weather Review, 147(6), 2283–2306. https://doi.org/10.1175/MWR-D-18-0330.1

Torralba, V., Doblas-Reyes, F. J., & Gonzalez-Reviriego, N. (2017). Uncertainty in recent near-surface wind speed trends: A global reanalysis intercomparison. Environmental Research Letters, 12(11), 114019. https://doi.org/10.1088/1748-9326/aa8a58

Tucker, S. C., Senff, C. J., Weickmann, A. M., Brewer, W.A., Banta, R. M., Sandberg, S. P., Law, D.C., & Hardesty, R.M. (2009). Doppler lidar estimation of mixing height using turbulence, shear, and aerosol profiles. J. Atmos. Ocea. Tech. 26(4), 673 – 688. https://doi.org/10.1175/2008JTECHA1157.1

Vose, R. S., Applequist, S., Bourassa, M. A., Pryor, S. C., Barthelmie, R. J., Blanton, B., et al., (2014). Monitoring and understanding changes in extremes: Extratropical storms, winds, and waves. Bulletin of the American Meteorological Society, 95(3), 377–386. https://doi.org/10.1175/BAMS-D-12-00162.1

Wandishin, M. S., Stensrud, D. J., Mullen, S. L., & Wicker, L. J. (2010). On the predictability of mesoscale convective systems: Three-dimensional simulations. Monthly Weather Review, 138(3), 863–885. https://doi.org/10.1175/2009MWR2961.1

Weisman, M. L. (1992). The role of convectively generated rear-inflow jets in the evolution of long-lived mesoconvective systems. J. Atmos. Sci., 49, 1826–1847. https://doi.org/10.1175/1520-0469(1992)049<1826:TROCGR>2.0.CO;2

Weisman, M. L., & Davis, C. A. (1998). Mechanisms for the generation of mesoscale vortices within quasi-linear convective systems. J. Atmos. Sci., 55, 2603 – 2622. https://doi.org/10.1175/1520-0469(1998)055<2603:MFTGOM>2.0.CO;2

Weisman, M. L., & Trapp, R. J. (2003). Low-level mesovortices within squall lines and bow echoes. Part I: Overview and dependence on environmental shear. Mon. Wea. Rev., 131, 2779 – 2803. https://doi.org/10.1175/1520-0493(2003)131<2779:LMWSLA>2.0.CO;2

Wilson, J. W., Feng, Y., Chen, M., & Roberts, R. D. (2010). Nowcasting challenges

https://doi.org/10.5194/egusphere-2025-5371
Preprint. Discussion started: 7 November 2025

during the Beijing Olympics: Successes, failures, and implications for future nowcasting systems, Weather Forecast., 25, 1691 – 1714. https://doi.org/10.1175/2010WAF2222417.1

Wheatley, D. M., & Trapp, R. J. (2008). The effect of mesoscale heterogeneity on the Genesis and structure of mesovortices within quasi-linear convective systems. Monthly Weather Review, 136(11), 4220-4241. https://doi.org/10.1175/2008MWR2294.1.

Wu, L., H. Su, X. Zeng, D. J. Posselt, S. Wong, S. Chen, and A. Stoffelen, (2024). Uncertainty of Atmospheric Winds in Three Widely Used Global Reanalysis Datasets. J. Appl. Meteor. Climatol., 63, 165 – 180, https://doi.org/10.1175/JAMC-D-22-0198.1.

Xiao, X, Sun, J., Chen, M. X., Qie, X., Wang, Y., & Ying, Z. M. (2017). The characteristics of weakly forced mountain-to-plain precipitation systems based on radar observations and high-resolution reanalysis, J. Geophys. Res.-Atmos., 122, 3193 – 3213.

Xiao, X, Sun, J., Chen, M. X., Qie, X., Ying, Z. M., Wang, Y., & Ji, L. (2019). Comparison of environmental and mesoscale characteristics of two types of mountain-to-plain precipitation systems in the Beijing region, China, J. Geophys. Res.-Atmos., 124, 6856 – 6872.

Xu, X., Xue, M., & Wang, Y. (2015a). The genesis of mesovortices within a real-data simulation of a bow echo system. J. Atmos. Sci., 72, 1963 – 1986. https://doi.org/10.1175/JAS-D-14-0209.1

Xu, X., Xue, M., & Wang, Y. (2015b). Mesovortices within the 8 May 2009 bow echo over the central United States: Analyses of the characteristics and evolution based on Doppler radar observations and a high-resolution model simulation. Mon. Wea. Rev., 143, 2266 – 2290. https://doi.org/10.1175/MWR-D-14-00234.1

Xu, X., and Coauthors (2024). Dynamics of Two Episodes of High Winds Produced by an Unusually Long-Lived Quasi-Linear Convective System in South China. J. Atmos. Sci., 81, 1449 – 1473. https://doi.org/10.1175/JAS-D-23-0047.1

https://doi.org/10.5194/egusphere-2025-5371
Preprint. Discussion started: 7 November 2025

995 Yanai, M., & Nitta, T. (1967). Computation of vertical motion and vorticity budget in
996 a Caribbean easterly wave, J. Meteor. Soc. Japan, 45, 444 – 466.
997 Zhang, D.-L., & Gao, K. (1989). Numerical simulation of an intense squall line during
998 10 – 11 June 1985 PRE-STORM. Part II: Rear inflow, surface pressure
999 perturbations and stratiform precipitation. Monthly Weather Review, 117(9),
1000 2067 – 2094.
1001 Zhang, L., Sun, J., Ying, Z., & Xiao, X. (2021). Initiation and development of a squall
1002 line crossing Hangzhou Bay. Journal of Geophysical Research: Atmospheres,
1003 126(1). https://doi.org/10.1029/2020JD032504
1004 Zhou, A., Zhao, K., Lee, W.-C., Huang, H., Hu, D., & Fu, P. (2020). VDRAS and
1005 polarimetric radar investigation of a bow echo formation after a squall line merged
1006 with a preline convective cell. J. Geophys. Res. Atmos., 125, e2019JD031719.
1007 https://doi.org/10.1029/2019JD031719.
1008 Zhou, X., Zhang, C., Xiao, Z., Li, Y., & Lu, G. (2025). Inverse Energy Cascades in the
1009 Boundary Layer During Strong Winds Based on Doppler Lidar. Geophysical
1010 Research Letters, 52(2). https://doi.org/10.1029/2024GL113273
1011

https://doi.org/10.5194/egusphere-2025-5371
Preprint. Discussion started: 7 November 2025

Figures

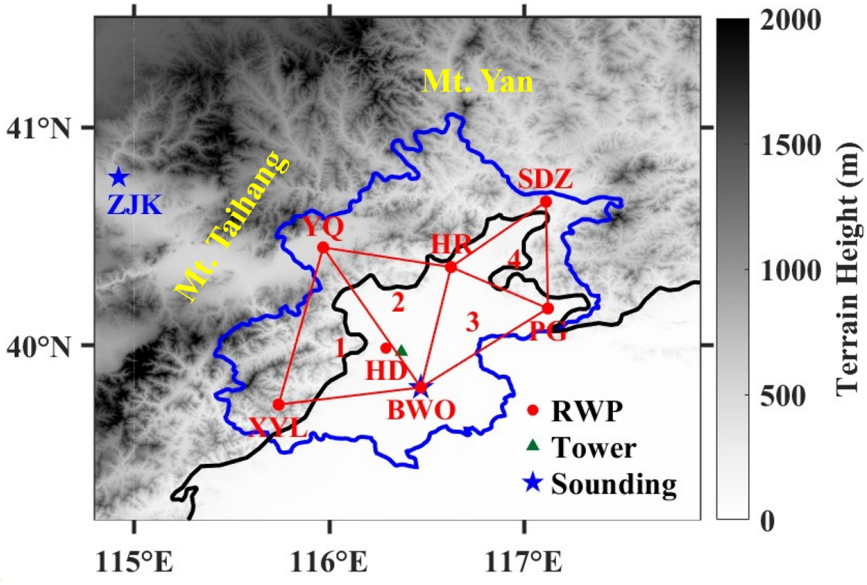

Figure 1. Spatial distribution of the terrain height over Beijing and surrounding areas with the black and blue line denoting the plain line at 200 m terrain elevation and the provincial boundaries, respectively. Seven RWPs (red dots) deployed at Xiayunling (XYL), Shangdianzi (SDZ), Huairou (HR), Yanqing (YQ), Haidian (HD), Pinggu (PG), and the Beijing Weather Observatory (BWO). Four red triangles with number denote the regions used to calculate the dynamic parameters with the triangle method. Blue five-pointed stars denote the L-band sounding at BWO and Zhangjiakou (ZJK) station. Green small triangle represents the location of meteorological tower.

https://doi.org/10.5194/egusphere-2025-5371
Preprint. Discussion started: 7 November 2025

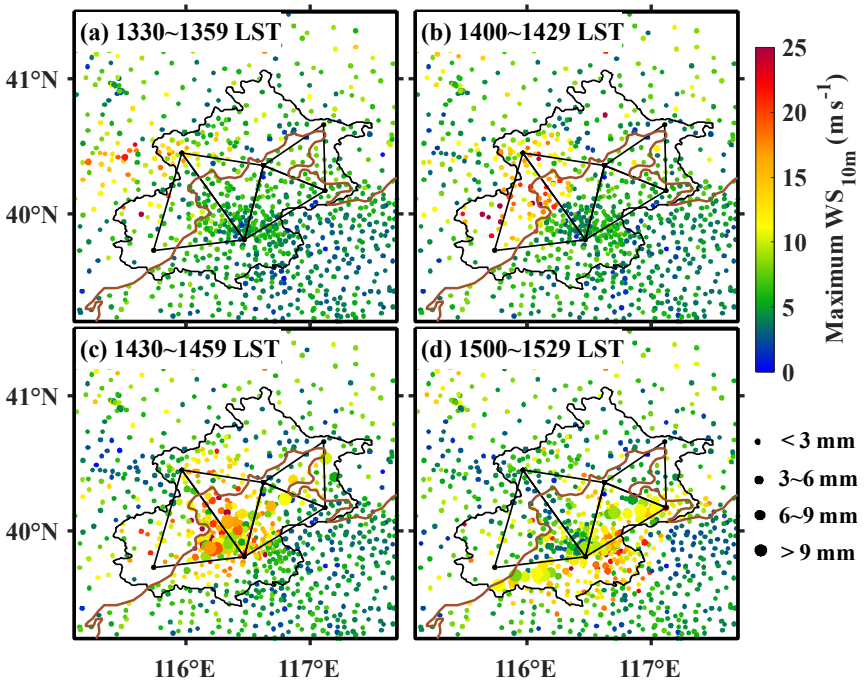

Figure 2. Maximum 10 m wind speed (shading of dots, m s^{-1}) observed during (a) 1330-1359 LST, (b) 1400-1429 LST, (c) 1430-1459 LST, and (d) 1500-1529 LST. The size of dots denoted the accumulated rainfall in 30 minutes.

https://doi.org/10.5194/egusphere-2025-5371
Preprint. Discussion started: 7 November 2025

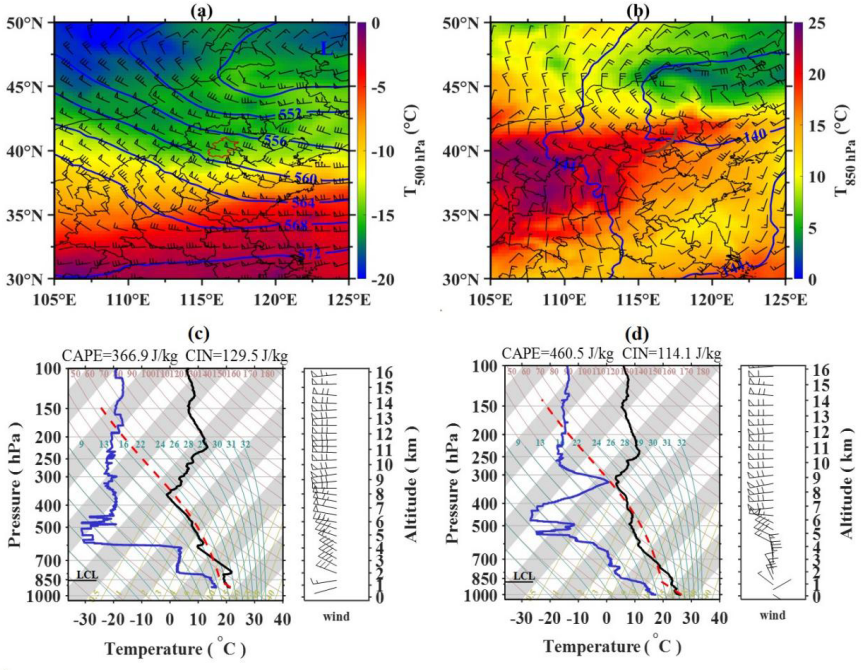

Figure 3. Horizontal distribution of temperature (color-shaded; °C), geopotential height (solid blue lines; 10 gpm) and wind barbs (a full barb is 4 m s^{-1} with a flag denoting 20 m s^{-1}) at (a) 500 hPa and (b) 850 hPa from the ERA5 hourly reanalysis data at 1400 LST on 30 May 2024. Note that the administrative boundary of Beijing is marked in red curve, the letter L denotes the center of a low-pressure system, and the skew T-log P diagrams derived from the upper-air sounding at the ZJK (c) and BWO (d) site at 0800 LST on 30 May 2024.

https://doi.org/10.5194/egusphere-2025-5371
Preprint. Discussion started: 7 November 2025

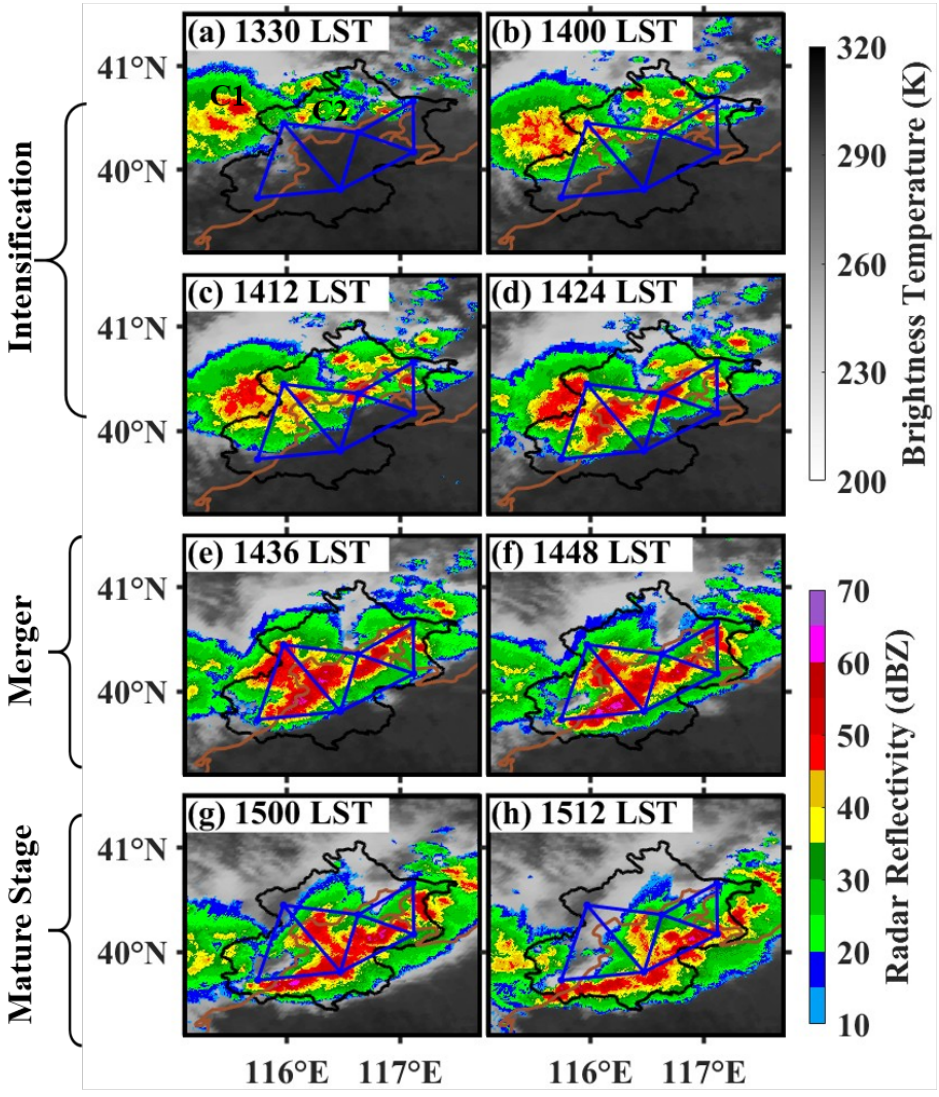

Figure 4. Brightness temperature from 10.8 μm channel of Himawari-8 geostationary satellite (gray shadings; K), superimposed with composite radar reflectivity (color-shaded; dBZ) at (a) 1330, (b) 1400, (c) 1412, (d) 1424, (e) 1436, (f) 1448, (g) 1500, and (h) 1512 LST on 30 May 2024. The four blue triangles and brown line denote the RWP mesonet and the 200 m terrain elevation line, respectively.

https://doi.org/10.5194/egusphere-2025-5371
Preprint. Discussion started: 7 November 2025

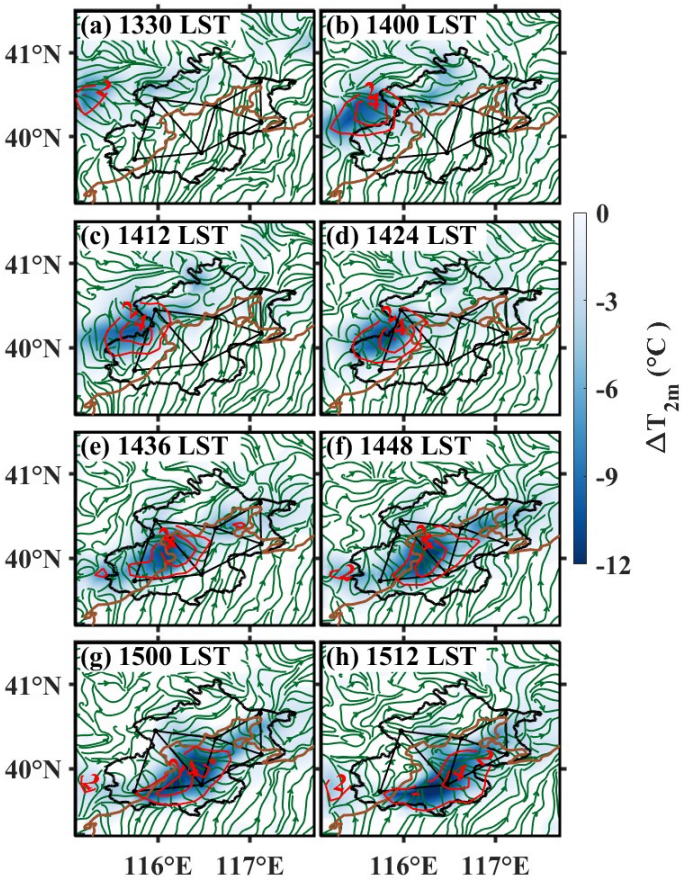

Figure 5. Evolution of T_{2m} change (color-shaded; °C) and pressure change (solid red lines at 2 hPa intervals) in 30 minutes, superimposed with 10 m streamlines derived from AWSs from (a) 1300 to (h) 1512 LST on 30 May 2024.

https://doi.org/10.5194/egusphere-2025-5371
Preprint. Discussion started: 7 November 2025

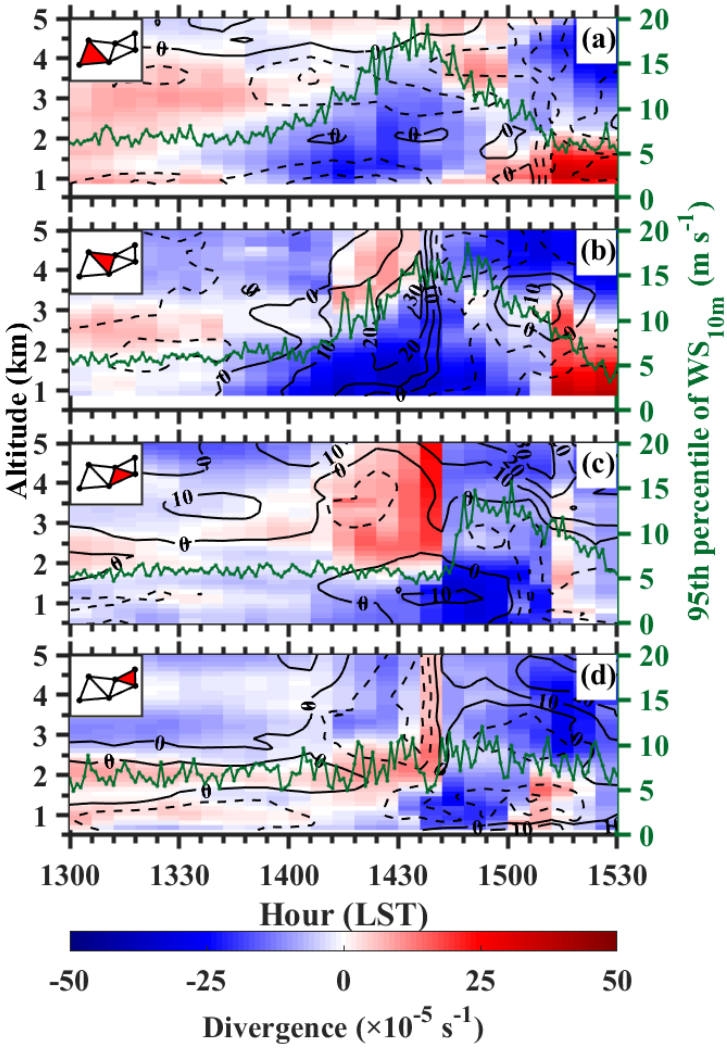

Figure 6. The vertical profiles of horizontal divergence (D, color shaded; s^{-1}) and vertical vorticity (ζ, dashed/solid contours for negative/positive values; s^{-1}) in (a) triangle 1, (b) triangle 2, (c) triangle 3, (d) triangle 4 derived from the RWP mesonet (see their locations as the red patches on the small maps in the upper left corners) from 1300 to 1530 LST on 30 May 2024. Green dotted lines show the 95th percentile of 10 m wind speed for all stations in the triangle area at 1-min intervals.

https://doi.org/10.5194/egusphere-2025-5371
Preprint. Discussion started: 7 November 2025

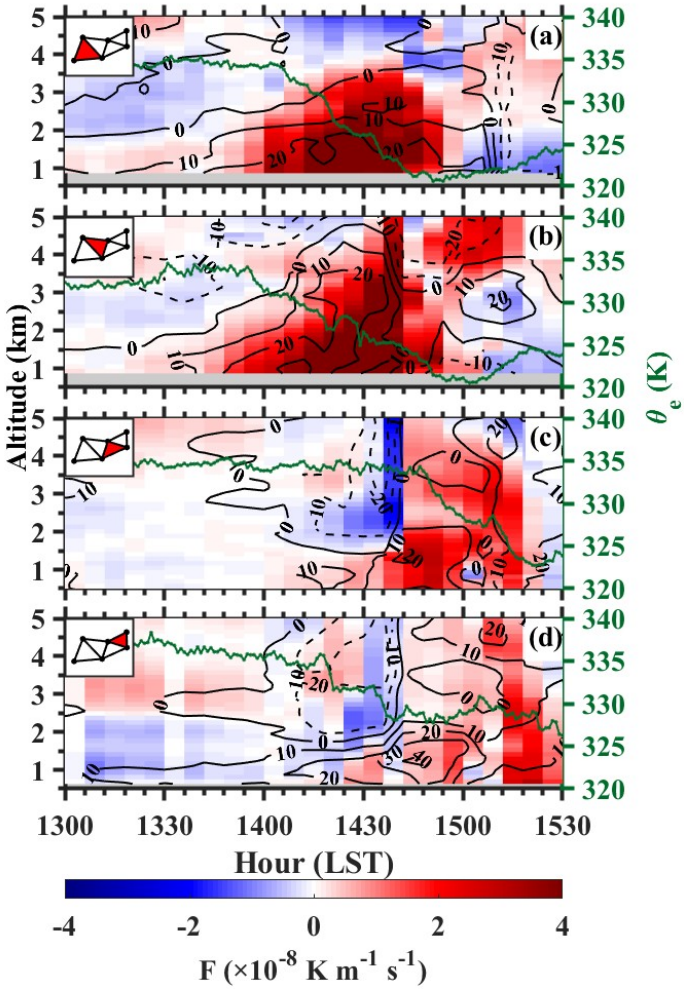

Figure 7. Same as Figure 6, except for frontogenesis function (F, color shaded; K m^{-1} s^{-1}) and shearing deformation (S; contours, s^{-1}). Green dotted lines show the area-averaged equivalent potential temperature θ_e (K) for all stations in the triangle area at 5-min intervals.

https://doi.org/10.5194/egusphere-2025-5371
Preprint. Discussion started: 7 November 2025

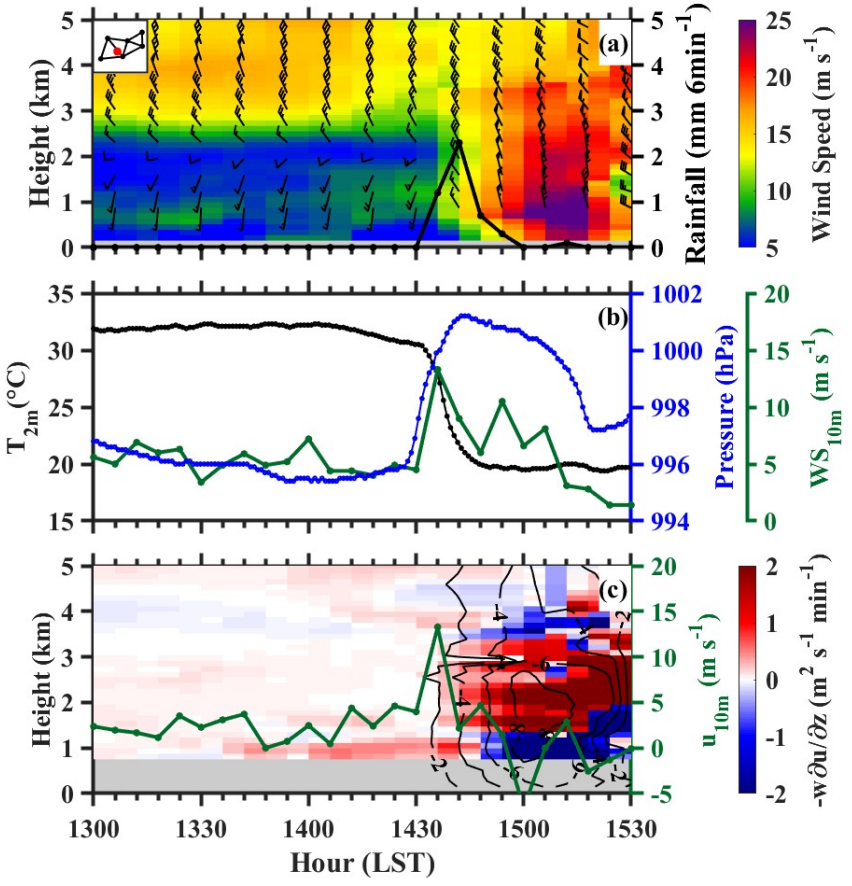

Figure 8. (a) Vertical profiles of horizontal wind barbs between 0 and 5 km height, superimposed with horizontal wind speed (shadings; m s-1) at HD (see its location as red dots on the small maps in the upper-left corners) during the period of 1300-1530 LST on 30 May 2024. The black solid line shows 6-min accumulated precipitation (mm $6min^{-1}$). (b) Time series of 2m temperature (°C) in black, instantaneous 10 m wind speed (m s^{-1}) in green, and pressure (hPa) in blue at HD; (c) Vertical advection of u component of horizontal wind, $-w\partial u/\partial z$ (shading, m^2 s^{-1} min^{-1}) superimposed with vertical velocity (contours, m s^{-1}) at HD. The green solid line shows u component of instantaneous 10 m wind (m s^{-1}).

https://doi.org/10.5194/egusphere-2025-5371
Preprint. Discussion started: 7 November 2025

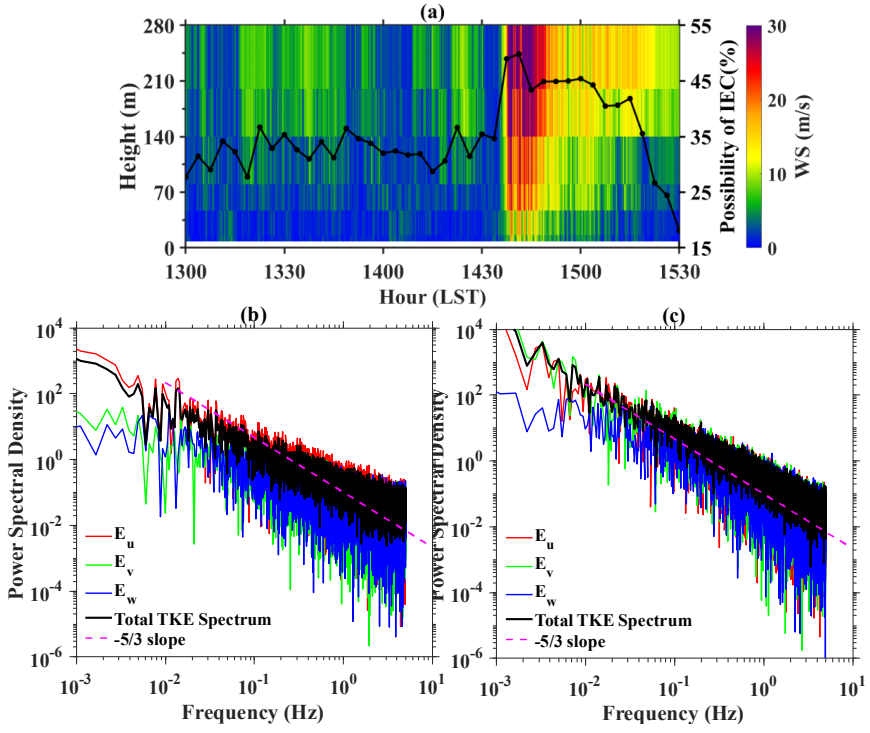

Figure 9. (a) Vertical profiles of horizontal wind speed (shadings; m s^{-1}) at the height of 8, 15, 47, 80, 140, 200 and 280 m during the period of 1300-1530 LST on 30 May 2024, which is directly measured from the meteorological tower (see its location in Figure 1) built and operated **by** the Institute of Atmospheric Physics, Chinese Academy Sciences. The black solid line shows the possibility of inverse energy cascades (IEC) at all heights. Energy spectra at the height of 280 m for components in different directions (u, v, w) during (b) 1406-1436 LST and (c) 1436-1506 LST, respectively. Dashed magenta line represents the theoretical Kolmogorov' s inertial range slope -5/3 in frequency domain.

https://doi.org/10.5194/egusphere-2025-5371
Preprint. Discussion started: 7 November 2025

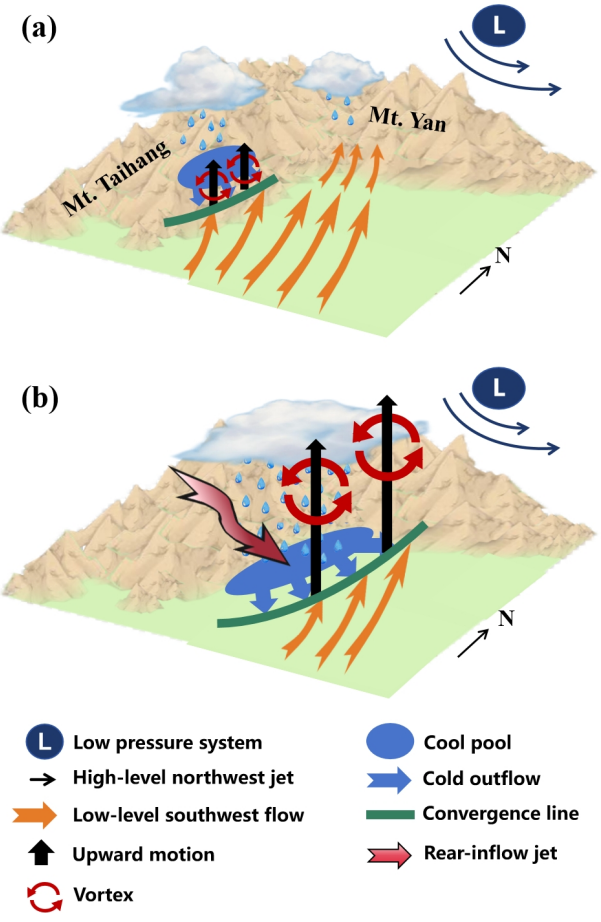

Figure 10. Conceptual model for the generation and evolution of near-surface high winds (a) before and (b) after the merger of the quasi-linear convective system (QLCS) in the extreme wind gust event in Beijing that occurred during the early afternoon of May 30, 2024.